PRESSURE VESSEL RESEARCH COUNCIL
OF THE
WELDING RESEARCH COUNCIL

Detonation-Induced Dynamic Pressure Loading in Containment Vessels

Thomas A. Duffey
Edward A. Rodriguez
Christopher Romero

Los Alamos National Laboratory

LA-UR-03-0741

January 2003

Report Submitted to:

Committee on Dynamic Analysis and Testing
Pressure Vessel Research Council
Welding Research Council

EXECUTIVE SUMMARY

The DynEx Project at Los Alamos National Laboratory (LANL) has the overall responsibility for design, analysis, manufacture, and implementation of new high-strength low-alloy (HSLA) steel spherical vessels to confine explosion products and debris from detonations of high-explosive (HE) assembly experiments.

Issues associated with the differences between transient and static pressures and their influences on structural response are addressed in this paper. The dynamic pressure loading acting on the LANL designed Confinement Vessel is described. The impulsive nature of the dynamic pressure loading of the confinement vessel is discussed and contrasted with static pressure loading. Asymmetric blast loading is discussed.

Following an introduction to the general subject of impulsive loading, structural dynamics loading concepts are presented. A section is also included on asymmetric blast loading that is due to an off-center charge or off-center initiation. Lastly, HE detonation effects are discussed from the standpoint of structural design with an introductory section on shock physics.

ACRONYMS AND SYMBOLS

ASME	American Society of Mechanical Engineers
DLF	Dynamic load factor
DoD	U.S. Department of Defense
DOE	U.S. Department of Energy
E	Specific internal energy
F	Force, (N or lb)
g	Gravitational constant, (m/s^2 or in/s^2)
H_{Exp}^{d}	Heat of detonation of high explosive, (ft-lb/lb)
H_{TNT}^{d}	Heat of detonation of TNT, (ft-lb/lb)
HE	High explosive
I_r	Positive normal reflected impulse, (psi-ms)
I_s^+	Positive phase impulse, (psi-ms)
I_s^-	Negative phase impulse, (psi-ms)
K, k	Spring stiffness, (N/m or lb/in)
M, m	Mass, (kg or lb)
ODE	Ordinary differential equation
P	Pressure, (MPa or lb/in^2 (psi))
P_o	Ambient pressure, (psi)
P_r	Peak positive normal-reflected pressure, (psi)
P_s^+	Positive peak overpressure (positive phase of blast wave), (psi)
P_s^-	Partial vacuum (negative phase of blast wave), (psi)
R	Distance to structure from center of high explosive, (ft)
SDOF	Single degree of freedom
U	Shock velocity, (km/s)
u	Particle velocity, (km/s)
t_a	Arrival time of blast wave to structure, (ms)
t_d^+	Duration of positive phase blast wave (ms)
t_d^-	Duration of negative phase blast wave, (ms)

ΔT, t_d	Duration of dynamic impulse, (ms)
T	Temperature (K)
W	Weight, (N or lb)
W_{Exp}	Weight of HE, (lb)
W_{TNT}	Weight of TNT, (lb)
Z	Scaled Distance ($ft/lb^{1/3}$)

Greek Symbols

ε_{ult}	Ultimate strain
$\varepsilon_{\max}$	Maximum strain
δ	Displacement, (in)
ρ	Density, (g/cm^3 or $lbf\text{-}sec^2/in^4$
σ	Nominal stress, (psi)
σ_o	Yield strength, (psi)
σ_{ys}	Static yield strength, (psi)
τ	Period of structural response, (ms)

TABLE OF CONTENTS

Detonation-Induced Dynamic Pressure Loading in Containment Vessels

by
T. A. Duffey, E. A. Rodriguez, and C. Romero

October, 2002

ABSTRACT

Vessels used to contain the effects of high explosions are designed in a wide variety of shapes, sizes and materials. Los Alamos National Laboratory has used spherical pressure vessels to conduct high-explosive detonation experiments for over 30 years. The military's explosives ordnance demolition (EOD) community uses pressure vessels to destroy aged conventional and chemical munitions. Issues associated with the differences between transient and static pressures and their influences on the structural response of these vessels are addressed in this report. These issues are illustrated by reference to an example spherical containment vessel for containing high explosives (HE), but the concepts are generally applicable to containment vessels of any shape or construction. In the past, design of these containment vessels was typically accomplished by maintaining that the vessel's kinetic energy, developed from the detonation impulse loading, be equilibrated by the elastic strain energy inherent in the vessel. Within the last decade, designs have been accomplished utilizing sophisticated and advanced computer codes that address both the detonation hydrodynamics and the vessel's highly nonlinear structural response. Notwithstanding the past accomplishments, no industry design standard(s) or guidelines have ever been developed to address a complete and rational design philosophy for detonation impulse loading of a pressure vessel. Nevertheless, this document provides the basis for the nonlinear dynamic loading associated with HE detonations, the resulting nonlinear and highly complex vessel response, and the static loading associated with the residual quasi-static overpressure. Understanding the dynamic events under detonation conditions is the first step towards the development of rational pressure vessel design criteria. Ultimately, it is hoped that the American Society of Mechanical Engineers (ASME) Boiler and Pressure Vessel Code will adopt a vessel design standard for HE detonations.

1.0 INTRODUCTION

The purpose of this report is to document the types of dynamic and static pressure loading acting on a typical high explosive containment vessel system and to explain the differences between these two types of pressure loading, as related to vessel response. An existing spherical pressure vessel is used to illustrate the concepts. The discussion herein is generally applicable to explosive containment vessels of different geometry and construction as well. The example containment vessel is shown in Figure 1.1 with the high-explosive (HE) charge detonation occurring inside.

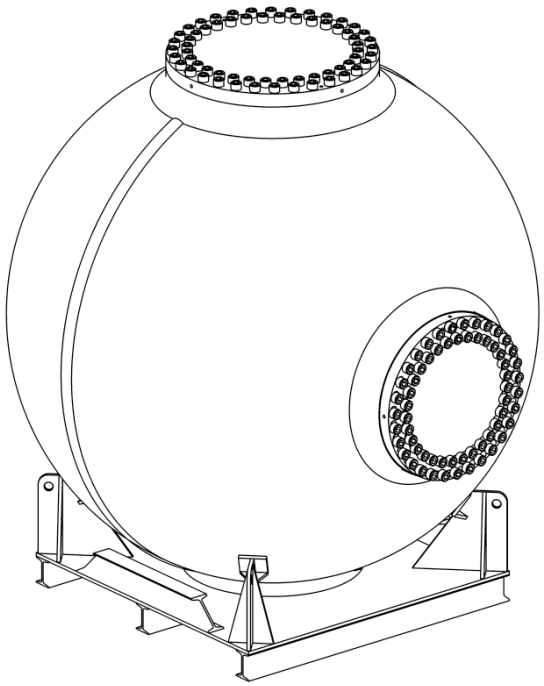

Figure 1.1. - Example 3-Port Spherical Containment Vessel

Use of a spherical pressure vessel to illustrate the dynamic loading and response principles is particularly relevant as a significant number of investigations have been reported in the open literature on the response of spherical shells or spherical containment vessels subjected to internal blast loading. However, it is important to note that non-spherical containment vessels, including vessels of cylindrical shape, are widely used as well.

A representative cross-section of containment vessels of various shapes and applications are presented in numerous references [1-10]. As discussed in [4], high-repetition vessel applications,

e.g., repeated testing of explosive components, are generally associated with linear-elastic only vessel designs. On the other hand, low-repetition vessel applications, such as containment of accidental explosions, are normally associated with elastic-plastic designs that efficiently utilize the plastic energy absorption capability of the vessel material.

A containment vessel is subjected to two distinct types of loading. First, following HE detonation, a shock wave is formed inside the vessel imparting a transient impulsive pressure loading to the vessel wall. Second, a long-term quasi-static pressure buildup occurs in the vessel due to the evolution and heating of gaseous detonation products. It is the impulsive loading, however, that is typically critical in the containment vessel design. The methods of analysis, as well as the vessel response, are distinctly different for the two types of loading experienced by the vessel.

A summary of structural dynamic loading concepts, as applied to containment vessels, and how these concepts compare with conventional ASME Code approach, is described in Section 2. Asymmetric blast loading associated with off-axis placement of HE is addressed in Section 3. Explosion phenomena are summarized in Section 4, first presenting a comparison between detonation and deflagration loading, second a brief summary of detonation physics is presented, and finally a description of empirical and analytical methods for determination of transient pressures under explosions is provided. A discussion of vibration modes of spherical Containment Vessels is presented in Section 5. Results and conclusions drawn from the evaluation are summarized in Section 6.

2.0 STRUCTURAL DYNAMICS LOADING CONCEPTS

The transient impulsive loading initially experienced by a containment vessel under HE loading is inherently different from static pressure loading. In order to understand these differences, it is necessary to review certain concepts regarding transient impulsive loading. These concepts are more fully discussed in classic references, such as Biggs [11]. These concepts are not used in conventional static pressure vessel analysis because inertia effects are not present for purely static loading. The purpose of this section is to demonstrate the generic differences in response that would be expected between static and dynamic pressure loading, with particular application to a containment vessel under impulsive loading.

2.1 Static versus Transient Impulsive Loading

For static pressure loading, the state of stress, strain, and deformation fields of a pressure vessel depend upon the magnitude of the applied pressure. The pressure is assumed to be sufficiently slowly applied such that the structure precisely tracks the loading, i.e., there is no dynamic overshoot. Stated differently, the inertia term in the equation(s) of motion of the structure plays no role in the overall response for purely static pressure loading.

A containment vessel is subjected to dynamic, impulsive pressure loading as a result of an internal HE detonation. The containment vessel is typically a simple structure (e.g., see Fig. 1.1) undergoing very complex response in a variety of vibration modes as a result of the dynamic pressure loading. The pressure-pulse loading on the inner vessel wall from the contained, HE detonation is also extremely complex. However, a good general understanding of the differences in vessel response between dynamic and static pressure loading can be gleaned by examining a simplified analytical model of both the structure and loading, as the fundamental response principles are identical. The fundamental differences between static and dynamic loading of the vessel will therefore be developed using a simple analytical model of the structure and loading. All solutions to be presented are readily obtained using conventional methods for solving second-order linear ordinary differential equations.

Consider a complete, point-symmetric spherical shell subjected to a spatially uniform internal pressure pulse, $p(t)$. The pulse is taken for simplicity as a rectangular pulse in time. However, for detonation (blast) loading, the actual pressure pulse is more akin to a step-function decaying with time. A segment of the spherical shell is shown in Fig. 2.1. The equation of motion for the "fundamental," or membrane breathing, mode of a thin shell is given by [12] :

$$\rho \frac{d^2 w}{dt^2} + \frac{2\sigma}{a} = \frac{p(t)}{h} \tag{2.1}$$

where ρ is mass density of the shell material, w is radial displacement (measured positive outward), a is the shell radius, h denotes shell thickness, σ is the balanced biaxial in-plane membrane stress, and t denotes time. Hooke's Law for a biaxial stress state is

$$\sigma = \frac{E}{1-\nu}\varepsilon \tag{2.2}$$

where E and ν denote Young's modulus and Poisson's ratio, respectively, and ε denotes the in-plane balanced biaxial strain in the shell, where

$$\varepsilon = \frac{w}{a} \tag{2.3}$$

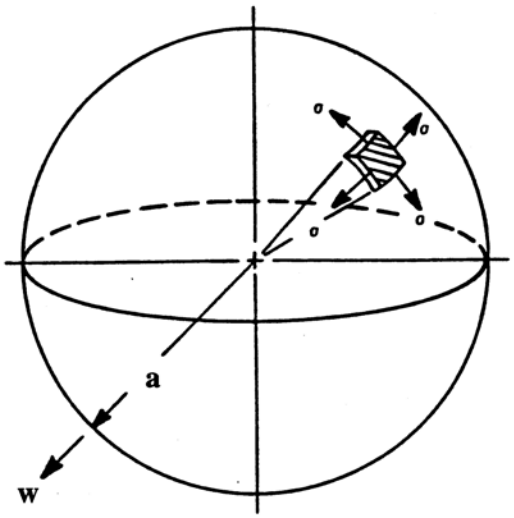

Figure 2.1. - Segment of a spherical shell [12].

Combining Eqns. (2.1) through (2.3) results in the following ODE governing one-dimensional, linearly elastic motion of a thin spherical shell:

$$\frac{d^2w}{dt^2} + \beta^2 w = \frac{p(t)}{\rho h} \tag{2.4a}$$

where

$$\beta^2 = \frac{2E}{\rho a^2(1-\nu)} \tag{2.4b}$$

Consider for simplicity a rectangular pressure pulse of magnitude p_o and duration ΔT, as shown in Figure 2.2, applied uniformly to the inner surface of the shell. For zero initial conditions on radial displacement and velocity of the shell, the solution of Eqn. (2.4a) for the rectangular pressure pulse is

$$w = \frac{p_0}{\rho h \beta^2}\left[1 - \cos \beta t\right] \qquad \text{for } t<\Delta T \qquad (2.5a)$$

and

$$w = \frac{p_0}{\rho h \beta^2}\left[1 - \cos \beta (t - \Delta T) - \cos \beta t\right] \qquad \text{for } t>\Delta T \qquad (2.5b)$$

Equations (2.5a) and (2.5b) provide the solution for radial displacement of the simplified model of the vessel as a function of time for the case of a rectangular pulse, from which peak displacement can be found. Again, the rectangular pulse was chosen here for simplicity to illustrate the physics. The corresponding strain-time solution is simply determined by substituting the displacement-time solution into Eqn. (2.3). Stress as a function of time is obtained by substituting the strain-time solution into Eqn. (2.2). Results in this report are presented in terms of peak displacements of the shell, but the same conclusions can be drawn using the corresponding strain or stress solutions. All simplified vessel peak displacement results presented in this report are determined from peak values obtained from Eqns. (2.5).

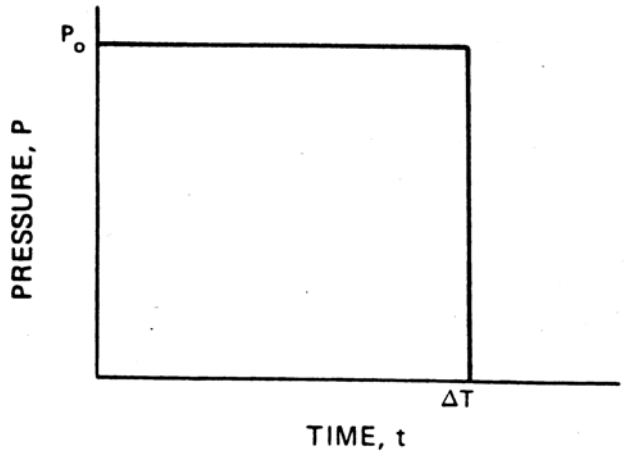

Figure 2.2. - Rectangular internal pressure pulse [12].

The solution in Eqns. (2.5) can be exploited in several ways to glean information on the role of the pressure pulse on peak radial displacement for in-plane stress and strain. First, however, two extreme loading cases are developed: A step pressure pulse, i.e., a pulse of magnitude, p_o, of infinite duration, and a pressure pulse of very high magnitude, but of extremely short duration.

2.2 Step Pressure Pulse

For $p(t) = p_o$, Eqn. (2.4) becomes

$$\frac{d^2 w}{dt^2} + \beta^2 w = \frac{p_0}{\rho h} \tag{2.6}$$

The solution of Eqn. (2.6) (with zero initial conditions) for radial displacement as a function of time is given for this step pressure pulse loading by

$$w = \frac{p_0}{\rho h \beta^2}(1 - \cos \beta t) \tag{2.7}$$

This solution is plotted in Fig. 2.3, where it is seen that the non-dimensional parameter $w\rho h\beta^2 / p_0$ oscillates between a value of 0 and 2. Also shown in Fig. 2.3 is the corresponding "static" solution for non-dimensional displacement of the shell of 1.0. This value can be readily obtained from Eqn. (2.6) by setting the inertia term to zero, resulting in the following equation:

$$w = \frac{p_0 a^2 (1 - \nu)}{2Eh} \tag{2.8}$$

This static solution corresponds to the case where the pressure, p_o, is applied very slowly, so there is no "dynamic overshoot." The factor of 2.0 corresponds to the fact that the pressure in Eqns. (2.6) and (2.7) is applied very rapidly. Therefore, a step pressure pulse results in a maximum dynamic load factor (DLF) of 2, that is, a step pressure pulse results in a displacement exactly twice the corresponding static solution to the same pressure magnitude.

The step pressure pulse solution corresponds to the extreme case where the pressure loading is applied in a time frame that is long in comparison to the response time of the vessel, i.e., the period of response, $2\pi / \beta$. The vessel response depends directly upon the pressure magnitude in this case. At the other extreme is the case where the pressure is applied extremely rapidly (relative to the response time of the vessel). That is, within the impulsive response regime, the

pressure loading is applied so rapidly that the entire loading is completed well before the shell has reached maximum deflection.

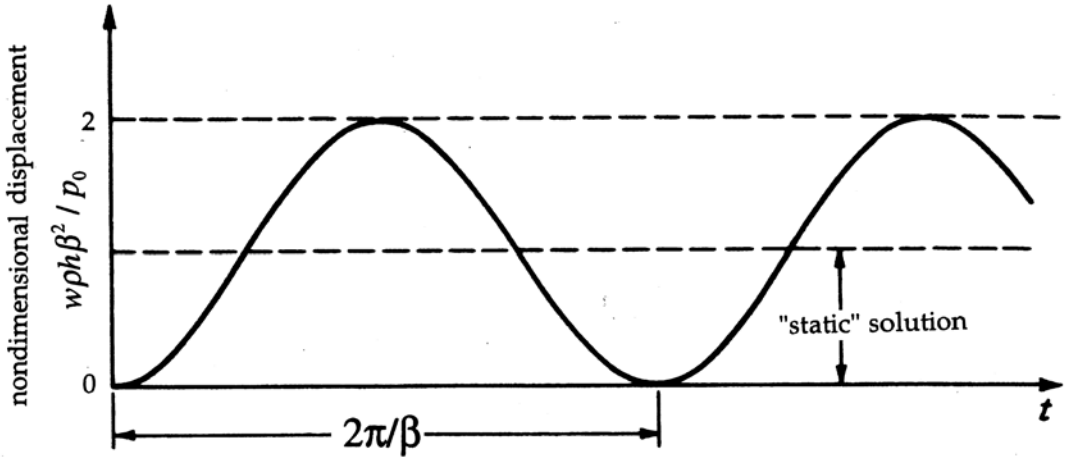

Figure 2.3. - Displacement-time history of spherical shell for a step pressure pulse (i.e., DLF=2.0).

2.3 Pure Impulse Solution

In the impulsive regime, the magnitude of the pressure, p_o, is of no direct consequence. Rather it is the impulse that governs dynamic and peak response of the vessel. The specific impulse (impulse per unit area), I, for a rectangular pulse is given by

$$I = \int_0^{\Delta T} p_0 dt = p_0 \Delta T \tag{2.9}$$

The impulsive solution can be developed from Eqn. (2.4) by representing the pressure as a Dirac Delta Function,

$$p(t) = I\delta(t) \tag{2.10}$$

or equivalently setting the pressure to zero and applying the impulsive loading as an initial velocity condition using the principle of impulse-momentum. In either case, the solution for radial displacement as a function of time is given by

$$w = \frac{I}{\rho h \beta} \sin \beta t \tag{2.11}$$

Equation (2.11) indicates that displacement response in the purely impulsive regime does not depend explicitly on the pressure magnitude, but rather on the area under the pressure-time curve.

In summary, dynamic and peak response of the simple vessel model for a rectangular pressure pulse is seen to depend upon the relative duration of pressure application, ΔT, and the period-of-response of the structure, $2\pi / \beta$. Denoting the period-of-response of the structure as τ, then the parameter $\Delta T / \tau$ appears key to the phenomenon of vessel response. For rapid pressure application, i.e., $\Delta T / \tau$ significantly less than 1, the response is impulsive and is given directly by Eqn. (2.11).

At the other extreme, $\Delta T / \tau$ significantly greater than 1, the solution depends only upon pressure magnitude, and Eqn. (2.7) directly applies. As was shown, application of a step pressure pulse results in a peak displacement exactly twice the corresponding static value. Between these two extremes lies a region where both pressure magnitude and specific impulse are important. It is, therefore, necessary to use Eqns. (2.5) for this intermediate region. That is, the limiting cases of Eqns. (2.5) approach both Eqns. (2.7) and (2.11).

There are several ways to present the above results of peak displacement of the vessel. First, the peak DLF for the peak vessel response as a function of the ratio of the rectangular pulse duration to the natural period of the vessel is shown in Fig. 2.4. Recall that the DLF is the ratio of peak dynamic vessel response to the static response to the same pressure. In Fig. 2.4, the magnitude of the pressure is held constant, but the pulse duration is varied. Again, the static solution corresponds to a DLF of 1.0. It can be seen that, for pressure pulses that are long compared to the period of the structure, the DLF approaches 2.0, as discussed above. At the other extreme, the DLF approaches zero. This result is a direct consequence of the fact that the peak pressure magnitude is being held constant.

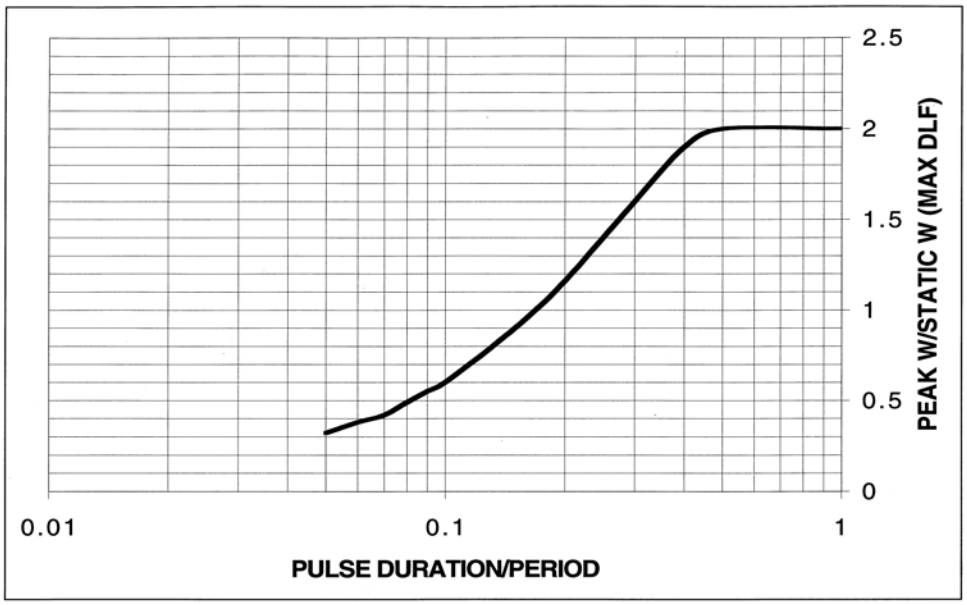

Figure 2.4. - Maximum dynamic load factor (DLF) as a function of $\Delta T / \tau$.

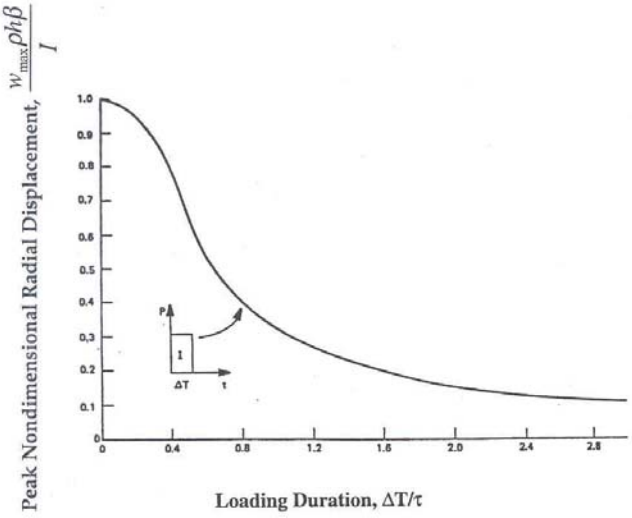

Figure 2.5. - Peak spherical shell response as a function of loading duration for a constant impulse [12].

Therefore, the impulse is monotonically decreasing as $\Delta T / \tau$ decreases. Fig. 2.4 demonstrates that for a given fixed value of peak pressure, the peak vessel response could vary anywhere from zero to a value corresponding to twice the static solution, depending on the duration of the loading. Clearly, using peak pressure alone in analyzing containment vessels is invalid.

An alternate way of presenting the implications of the above equations, in particular the peak values of Eqns. (2.5), is shown graphically in Fig. 2.5. Here, the specific impulse, I, i.e., the area under the pressure-time curve, is held constant while p_o and ΔT are simultaneously varied. The peak radial displacement, w_p, normalized with respect to the peak impulsive displacement, $I/\rho h\beta$, is plotted as a function of the loading duration in Fig. 2.5. This curve demonstrates that even if impulse is held constant, peak response of the vessel depends on the relative time of application of the loading. However, for pressure applied in a time frame that is short compared to the period of the vessel, peak response approaches the impulse solution asymptotically at the left side of Fig. 2.5.

As an approximate indication of the regime in which the example containment vessel of Fig. 1.1 operates, consider the following based on the above simplified model: For a 6-ft diameter, 2-in. wall HSLA-100 steel containment vessel subjected to a 10- and 20-lb HE detonation blast, a typical pulse duration, ΔT, is estimated at between 0.125 ms to 0.16 ms for the important part of the first pulse, whereas the vessel's period of vibration, τ, for the fundamental mode is 0.74 ms (or ~1350 Hz). The ratio $\Delta T / \tau$ is approximately 0.17 to 0.22, which places these particular containment vessels within the impulsive regime, as indicated in Fig. 2.5. The area under the pressure-time curve (i.e., the specific impulse), rather than the peak pressure itself, is the relevant parameter. The actual forcing function, i.e., pressure-time loading, experienced by the containment vessel is very complex. Structural response consists of a number of reverberations; i.e., not a single short pulse. However, the reverberations following the initial pressure peak are of little consequence to vessel response, providing at least some justification for the above use of a single pulse.

2.4 Containment Vessel Results

The above simple model sheds light on the role of pressure pulse loading and its relationship to static pressure loading. While the underlying principles governing dynamic response of the example containment vessel are identical to the simple model used above, confounding factors include vessel response not just in the fundamental "breathing" mode, but consisting of a large number of very complex modes, each with its own natural frequency. Moreover, other factors affecting the dynamic response of real Containment Vessels are discontinuities and changes of section (e.g., flanges and changes of shape) in which large bending stresses are introduced[1]. Details of the pressure pulse are also very complex. For example, determining a precise "pulse duration" is not a straightforward procedure.

2.4.1 Actual Pressure Pulse

A study performed by Martineau [13] using a detailed structural model of the example containment vessel determined the temporal location of the impulse-pressure spectrum where the actual vessel response lies. The study included a comparison of recorded pressure-time history from experimental data and the detailed dynamic FEA model.

The simulations performed by Martineau [13] were validated by experimental data for 10-lb and 20-lb HE charges using pressure sensors and bi-axial strain gages. The study demonstrates that the structural response of the vessel is determined primarily by the impulse of the pressure-time history and is not significantly dependent on the details of the pressure profile. The impulse analysis performed by Martineau to support his conclusions was as follows:

1. The dynamic pressure was calculated by the LANL shock-wave propagation hydrodynamics code, MESA-2D [14]. The pressure-time history was truncated after the first peak decayed to ambient and the specific impulse (area under the pressure-time curve) was determined.
2. Four other pressure pulses were then constructed with the same shock arrival time and impulse, but with different attributes, e.g., pulse duration and shape.
3. The first profile was assumed to be a simple triangular pulse. The second profile was of similar shape, but the duration of the pulse was reduced by 50%. The third profile was similar, but with duration increased to 150% of the first triangular pulse.
4. The fourth profile closely resembled a square wave.

The five pressure profiles are shown in Fig. 2.6. Each pressure profile was then used as input in performing separate computer simulations of the containment vessel response. The mathematical model and simulations were performed with the explicit structural dynamics finite element program, LS-DYNA [15], in which both membrane and bending effects are implicitly incorporated. The resulting vessel strain-time history (at one location) is shown in Fig. 2.7. The figure depicts that the dynamic response is nearly identical for each of the five pressure pulses.

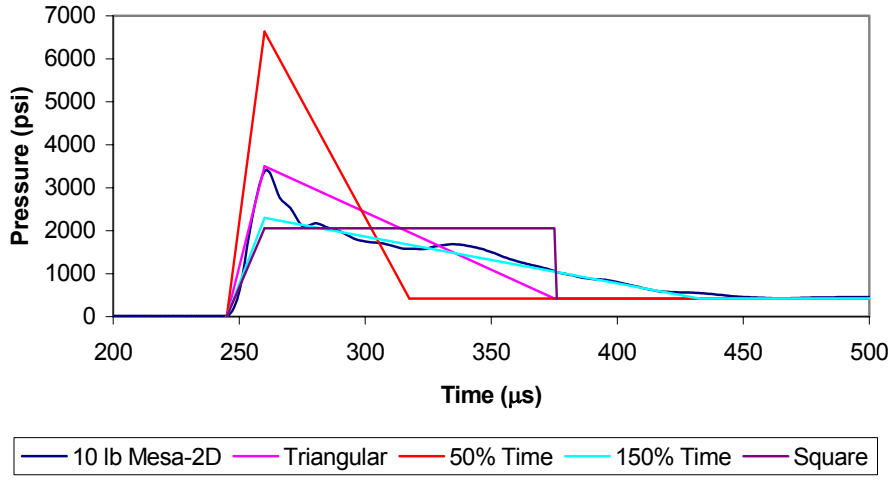

Figure 2.6. - Pressure profiles for impulse study [13].

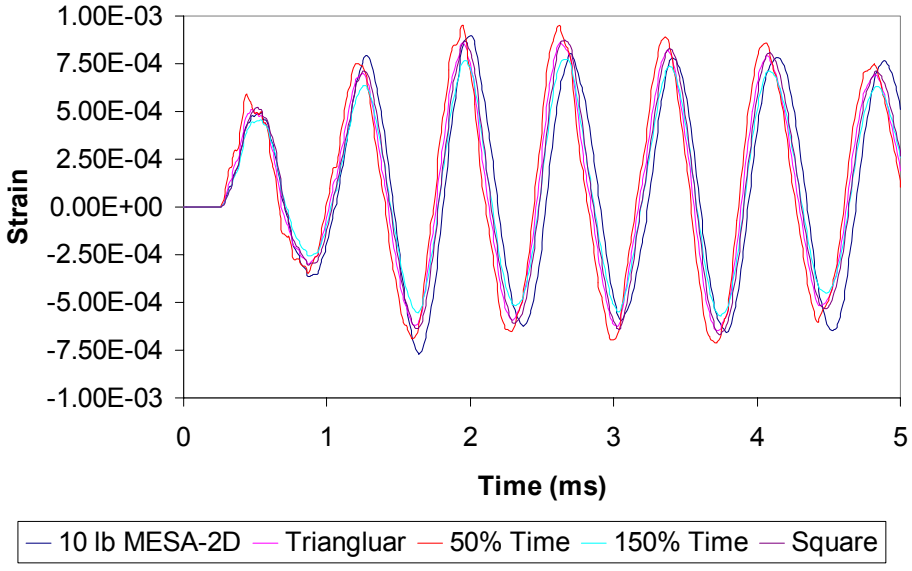

Figure 2.7. - Strain comparisons from impulse study [13].

Recalling that each of the pressure pulses has the same specific impulse, it is concluded that the dynamic response of the steel vessel is primarily dependent on the impulse of the pressure pulse and not on actual pulse details, such as peak pressure or pulse shape.

2.4.2 Vessel Response

The numerical analyses performed by Martineau [13] using LS-DYNA [15] show complex vessel responses, predominantly due to the large port masses. The source-term (forcing function or pressure-time history) for these results is shown on Figure 2.8, which is representative of a 40-lb of HE charge.

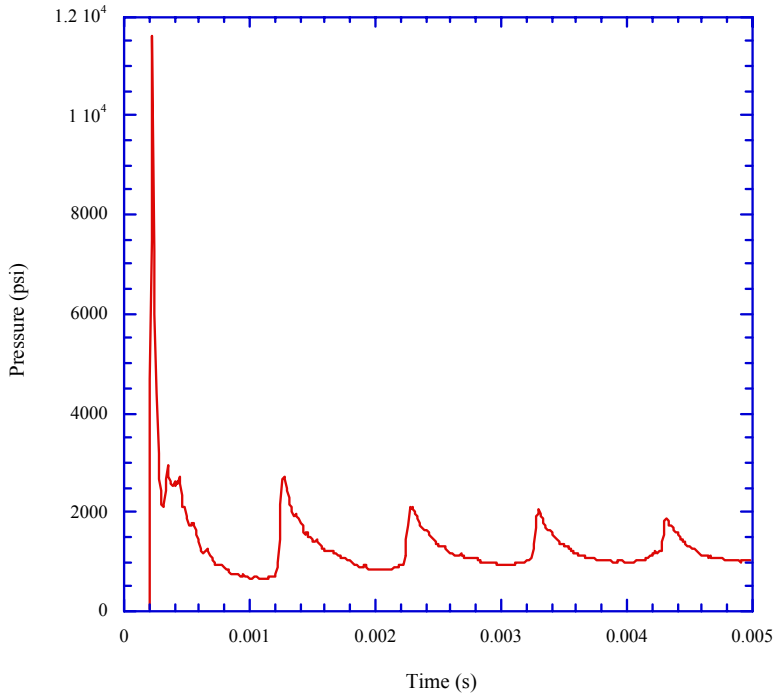

Figure 2.8. – Pressure-Time history for 40-lb HE

Figure 2.8 shows several decaying shock wave reverberations after the initial peak. These reverberations are indicative of the subsequent gas collapse and expansion phase, which follows the initial HE reaction products expansion at supersonic velocities. Figures 2.9 to 2.15 depict a time-sequence snapshot of the confinement vessel structural response to a detonation loading. Stress contours are in psi. These figures are based upon nonlinear time-history analysis.

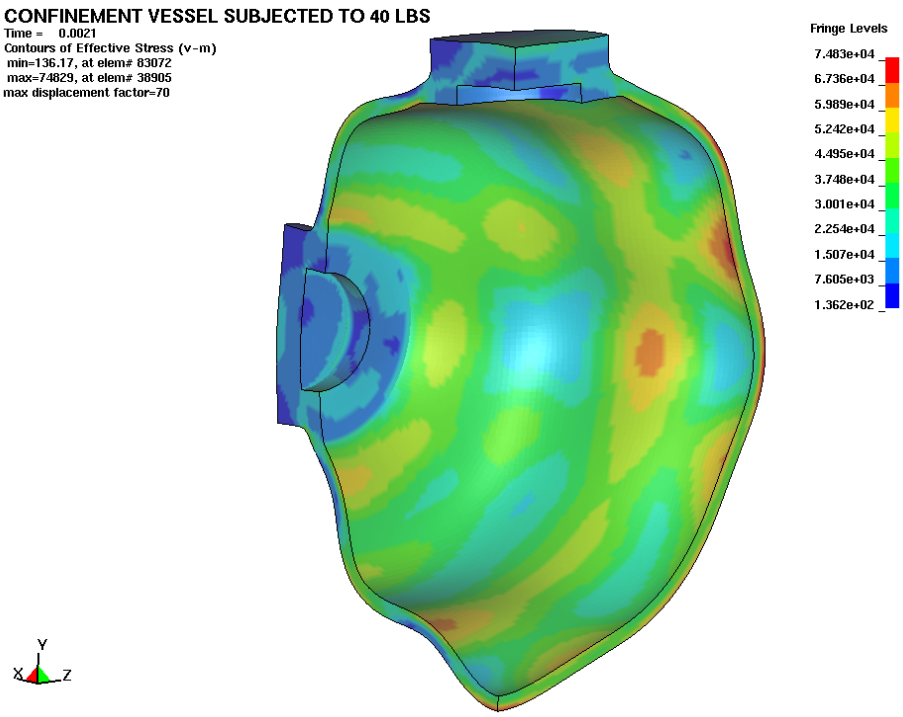

Figure 2.9 – Time = 2.1-ms

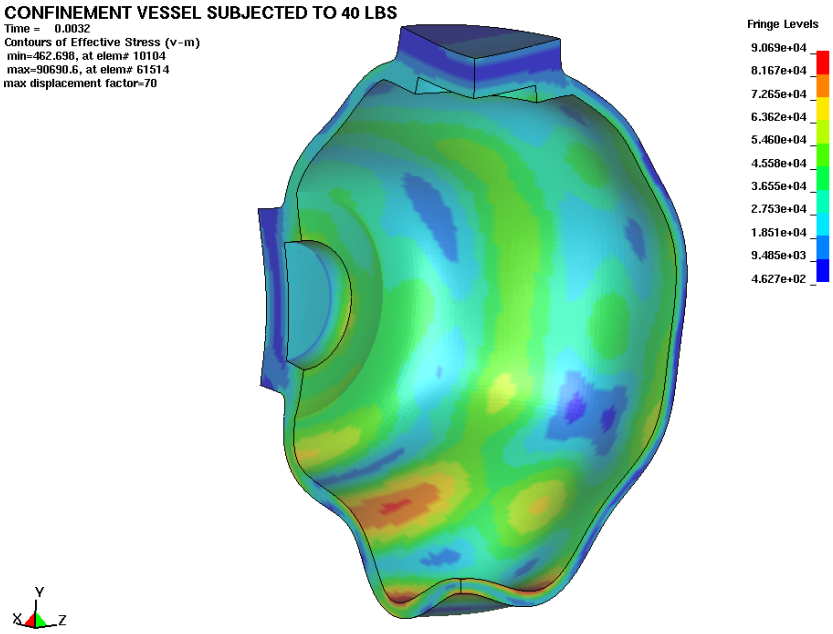

Figure 2.10 – Time = 3.2-ms

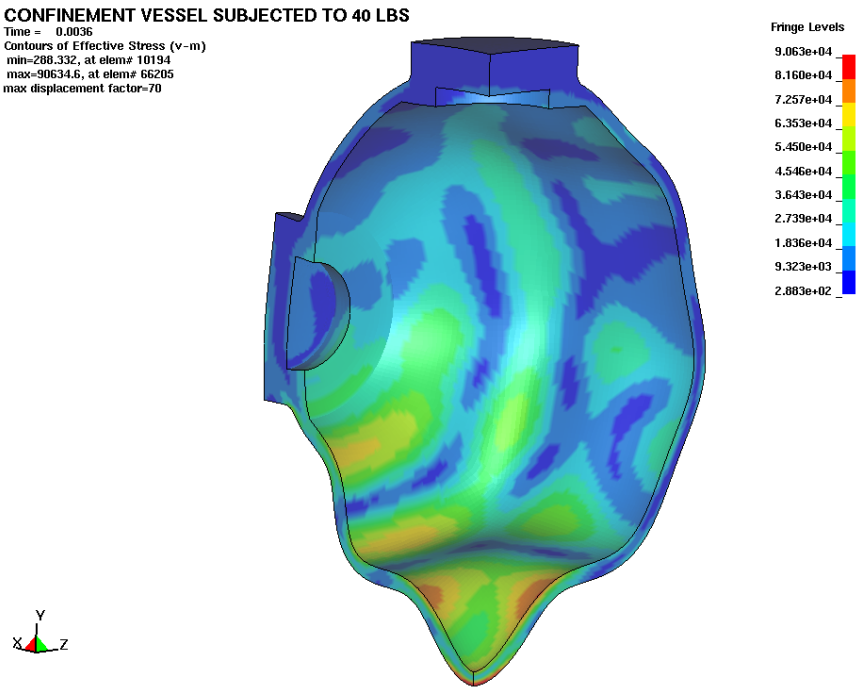

Figure 2.11 – Time = 3.6-ms

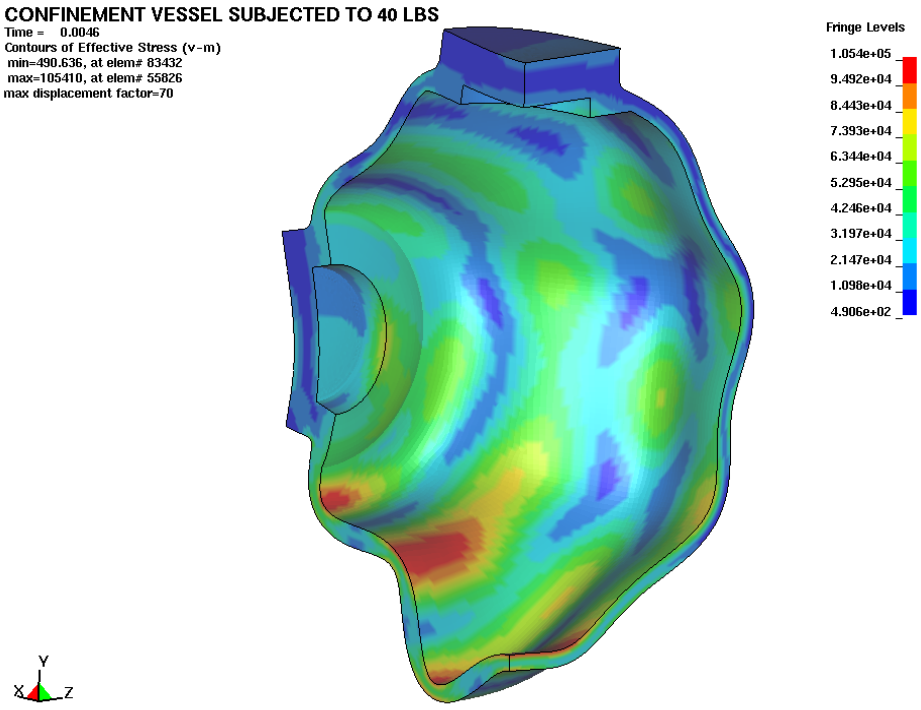

Figure 2.12 – Time = 4.6-ms

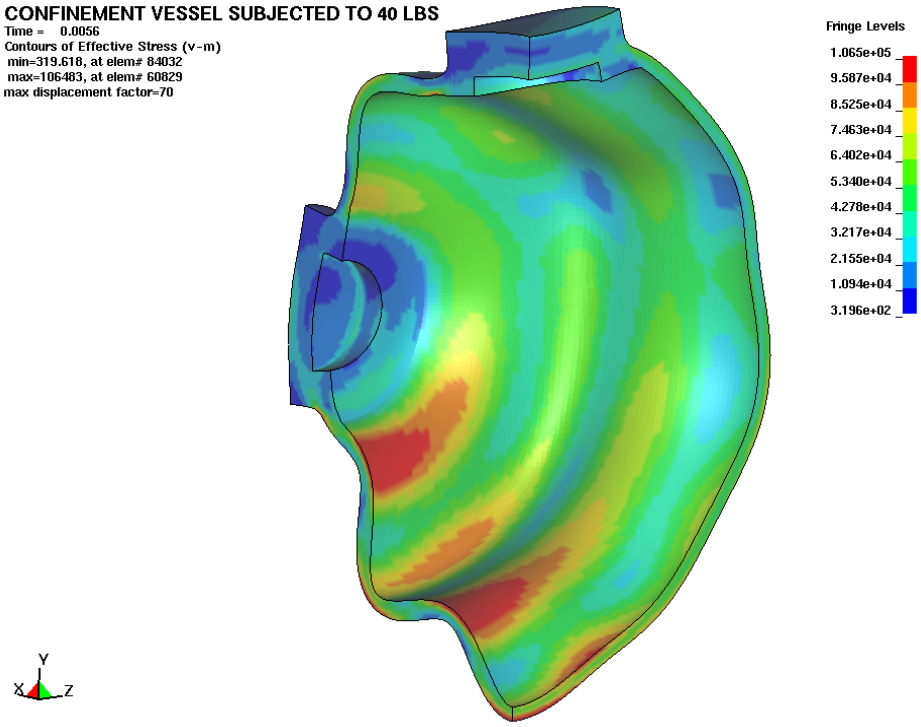

Figure 2.13 - Time = 5.6-ms

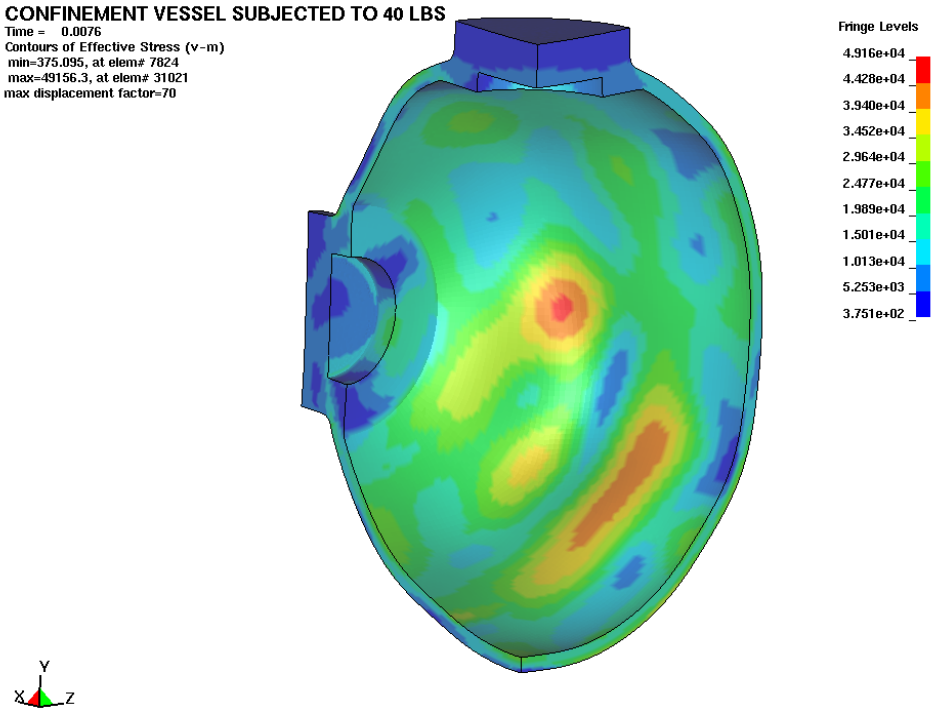

Figure 2.14 - Time = 7.6-ms

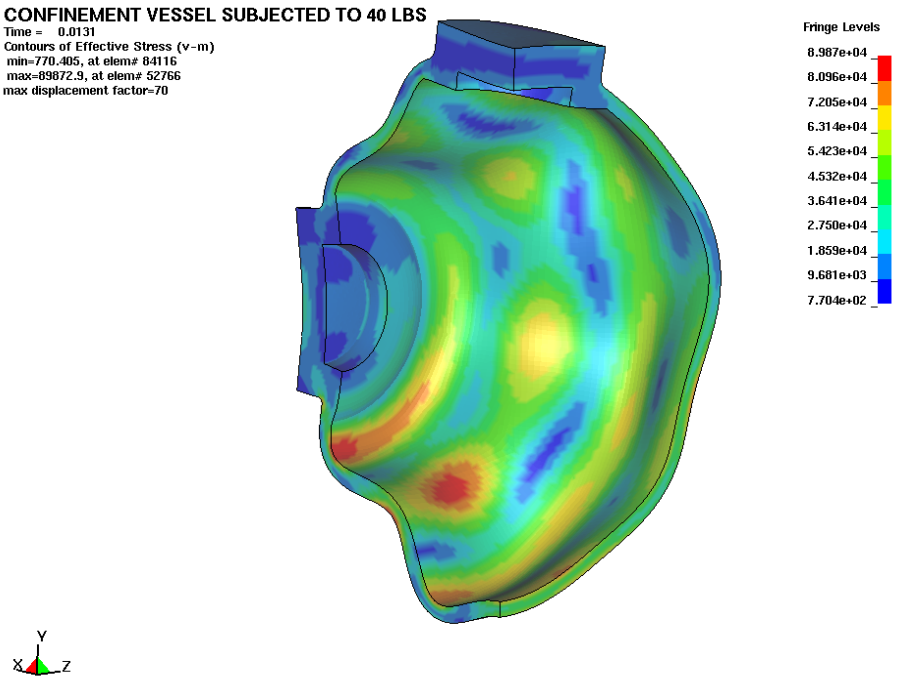

Figure 2.15 - Time = 13.1-ms

Of interest here is the temporal response at a particular location, e.g., transient principal stresses at the south pole of the vessel, superposed with the forcing function. This graphical representation provides a format for comparison of peak vessel response to impulse loading.

Figures 2.16a and 2.16b show that peak vessel response, e.g., maximum stress, occurs long after the initial pressure pulse has decayed. Details of Figure 2.16a show that HE initiation starts at 0-ms, followed by HE detonation at 15 μs (0.015-ms). At about 0.25-ms, the shock wave imparts on the vessel wall with an immediate pressure spike. The initial pressure peak decays within another 0.25-ms. At about 0.35-ms, the vessel begins to respond to the impulse load, with a "breathing" mode (i.e., n=0 mode) stress peaking at about 0.6-ms. However, Figure 2.16b shows peak vessel response (i.e., maximum stress) occurring at about 6-ms. Note that Figures 2.16a and 2.16b are intended only for comparisons of arrival times and durations of pressure loading and vessel response. Therefore, no units are shown on the ordinates of these curves.

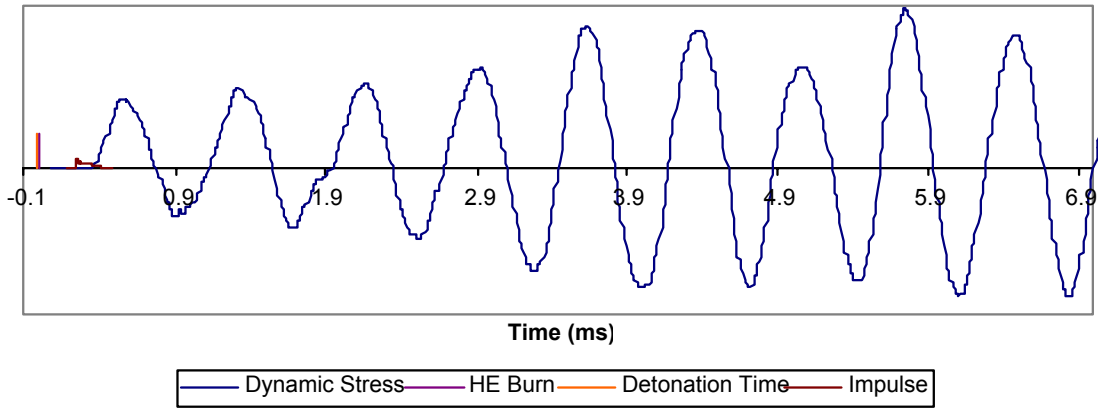

Figure 2.16a. – Vessel stress response superposed on impulse.

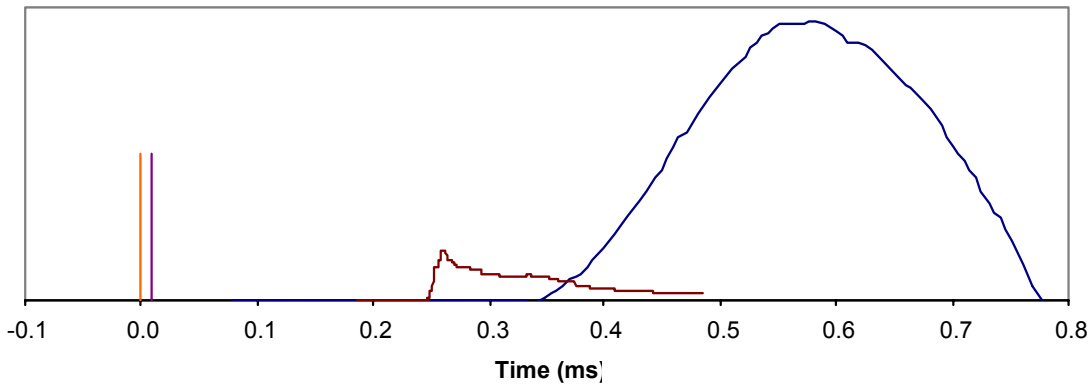

Figure 2.16b. – Close-up of initial vessel response superposed onto pressure pulse.

2.4.3 Experimental/Numerical Comparisons and Equivalent Step Pressure

A typical comparison of a strain-time history measured on the outer surface of the Containment Vessel with the corresponding Finite Element simulation is shown in Figure 2.17 [13]. It is seen that, at least out to 5 ms, agreement between the two strain-gage recordings and the Finite Element simulation is good. Moreover, the comparisons shown in Figure 2.17 are at the identical

location on the vessel as that used in the pressure pulse study presented in Section 2.4.1 (See Figure 2.7).

A comparison of Figure 2.17 with Figure 2.7 reveals that these curves are nearly identical. The implication is that the impulse associated with the initial pressure pulse (out to approximately 1 ms) primarily determines the transient structural response. The remaining impulse (i.e., from 1 ms to 7 ms) does not significantly affect the structural response because the remaining discrete impulses from the pressure-pulse reverberations provide little additional energy to the system. This is consistent with the impulse arguments presented in Section 2.4.1.

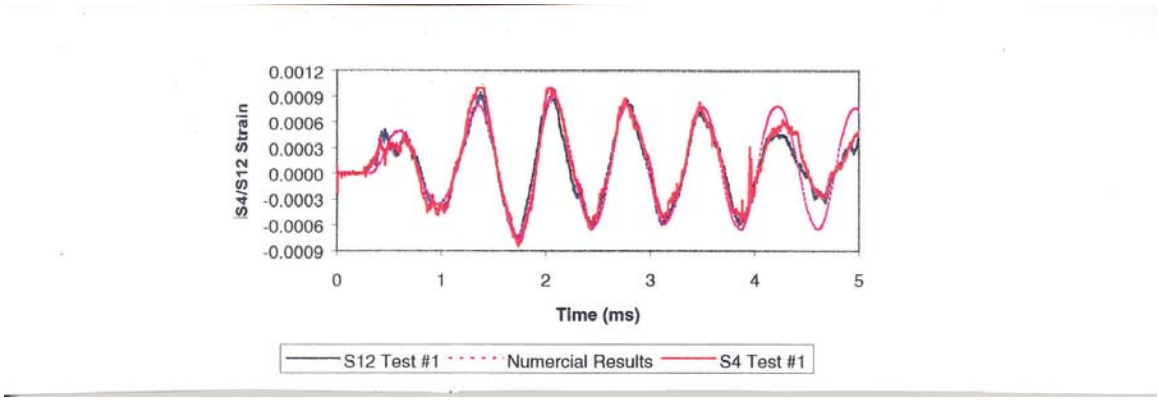

Figure 2.17 – Experimental/numerical strain-time comparison.

It is interesting to determine the magnitude of the step pressure pulse that would result in the same peak strains as the actual transient pressure pulse. The magnitude of this equivalent step pressure pulse is determined from the closed-form expressions for a perfect spherical shell given in Sections 2.2 and 2.3. A numerical (i.e., Finite Element) solution is avoided here for two reasons: 1) It is difficult to obtain a numerical solution for a true step pressure pulse, as the pulse must be applied as a steep ramp function; and 2) There would be a significant, misleading strain offset at late response times due to the high value of pressure applied for infinite time.

The single-degree-of freedom solutions presented in Sections 2.2 and 2.3 apply to the first (membrane) peak response of the Containment Vessel, and cannot account for the late-time strain buildup observed for the vessel discussed in Section 4. Starting with Equation (2.7) and noting that

$$\varepsilon = w/a$$

and

$$\beta^2 = \frac{2E}{\rho a^2 (1-\upsilon)}$$

then it is readily shown that the maximum (first cycle) strain is given by

$$\varepsilon_{\max} = \frac{P_0 a(1-\upsilon)}{Eh} \tag{2.12}$$

where all symbols are defined in Section 2.2.

Next, referring to the pure impulse solution given by Equation (2.11), it can be similarly shown that the maximum (first cycle) strain in this case is given by

$$\varepsilon_{\max} = \frac{I}{h}\sqrt{\frac{(1-\upsilon)}{2\rho E}} \tag{2.13}$$

The following input parameters are used for the Containment Vessel shown in Fig 1.1:

$$a = 37.0in$$
$$h = 2.50in$$
$$E = 29.9X10^6\ psi$$
$$\upsilon = 0.29$$
$$\rho = 7.32X10^{-4}\ lbf - \sec^2/in^4$$
$$I = 0.450\,psi - \sec$$

From Equation (2.13), the maximum, first cycle strain is estimated as $\varepsilon_{\max} = 7.34E-4in/in$. Comparing this value with the first peak strain in Figures 2.7 and 2.17 reveals that the approximate solution is within 15-percent of the experimental data and the Finite Element calculation for the Containment Vessel.

Now Equation (2.12) is solved for the equivalent step pressure pulse,

$$P_0 = \frac{\varepsilon_{\max} Eh}{a(1-\upsilon)} \tag{2.14}$$

Using the above input values and the maximum impulsive strain value calculated above, the equivalent step pressure magnitude is found to be

$$P_0 = 2030\,psi$$

This magnitude is approximately that shown in Figure 2.6 for the square pressure pulse.

3.0 INFLUENCE OF ASYMMETRIC BLAST LOADING

The above treatment for impulsive loading assumed a point-symmetric (spherical), center-initiated high-explosive charge that is centered in the spherical vessel. The spherical charge of high explosive may not be precisely centered in the vessel. In addition, it is possible to have a centered spherical charge that is not center-initiated. Also, HE detonations in non-spherical pressure vessels (i.e., cylinders or intersecting cylinders) will not attain a point-symmetric pressure loading. This geometrical asymmetry may be viewed as a perturbation in the geometry, whereas off-center placement or initiation of the charge may be viewed as a perturbation in the loading. The transient pressure loading in cylinders is quite complex owing to wave reflections from near surfaces, and rarefactions spreading in space. The influence of the resulting asymmetric pressure pulse loading on the inner wall of a spherical containment vessel is evaluated in this section for these two possibilities. It is concluded from the following that it is difficult to draw general conclusions regarding the influence of asymmetric blast loading. Asymmetric loading of Containment Vessels must be treated on a case-by-case basis.

3.1 Off-Center HE Initiation

The influence of off-center initiation of a centered spherical HE charge on peak vessel stresses and plastic strains was investigated by Stevens and Rojas [16] using the containment vessel configuration shown in Fig. 1.1. As described in [16], an elastic-plastic material model was utilized, based upon a linear segment fit to the true stress-true strain curve for the HSLA-100 vessel material. Strain rate effects were conservatively ignored. Computer simulations for centered spherical charges of 10-, 20-, and 40-lb HE were performed using an off-center initiation point, as depicted in Figure 3.1. Note that, in this case, the charge itself remains centered in the vessel. Pressure-time histories at 35 tracer points around the vessel were generated using CTH [17] for a half-symmetric model.

CTH is an Eulerian, hydrodynamic, shock wave propagation numerical code with equation-of-state capability developed by Sandia National Laboratories (SNL). The parallel version of the explicit Lagrangian DYNA-3D code, PARADYN, was used to develop the vessel structural model, using the output pressure-time histories from CTH as the input forcing functions. A measure of the influence of the off-center initiation is shown in Figure 3.2, a plot of the peak equivalent (von Mises) stress occurring in the vessel (for all vessel locations and response times) for both the center-initiated and off-center-initiated simulations. Results are shown for 10-, 20-, and 40-lb. HE.

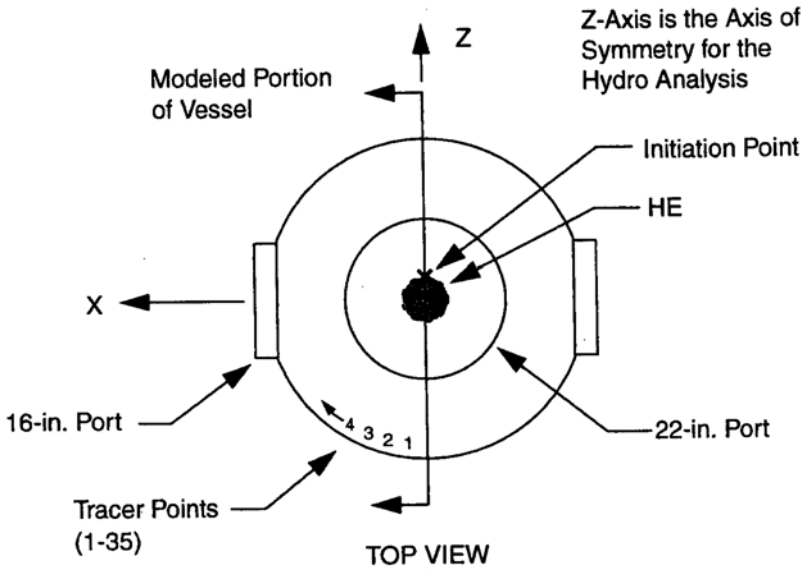

Figure 3.1. - Simulation of off-center initiation.

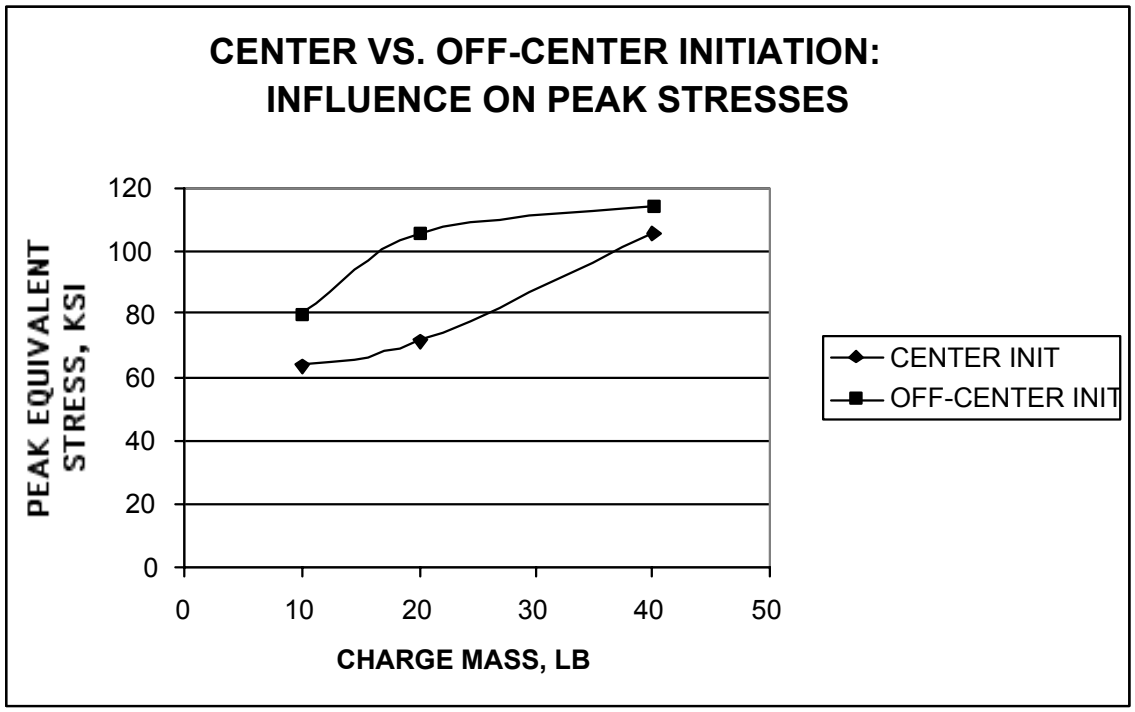

Figure 3.2. - Influence of off-center initiation on peak stresses.

Figure 3.2 demonstrates that the peak equivalent stress does increase substantially for off-center initiation.

3.2 Off-Axis HE Charge Placement

In the following, charge eccentricity is defined as the radial displacement of the charge from the center of the vessel divided by the vessel radius, i.e., eccentricity is defined as δ / R as shown in Figure 3.3. The first known attempt at evaluating the role of eccentric explosive source placement in elastic spherical shells was performed by Baker, Hu, and Jackson [5]. They reported a series of experiments with small explosive charges at eccentric positions and obtained qualitative agreement with their theory. Unfortunately, however, no general guidelines regarding the role of charge eccentricity were given.

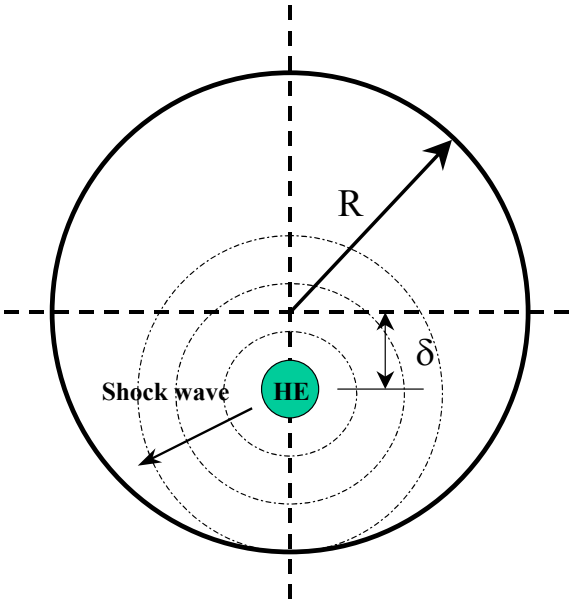

Figure 3.3. – Off-axis initiation/detonation.

Belov, et al., [18] reported on Russian containment vessel work using a vessel qualitatively similar to that shown in Fig. 1.1, but with only one nozzle port, located at the north pole. They present experimental results for the cases of central and eccentric charge locations. To create the eccentricity, the charge was moved along the vertical axis of the vessel in the direction of the south pole. Measurements of the strain at various locations on the shell outer surface were then made as a result of charge detonation.

The peak strain during the first half-period of shell vibration, ε_1, and the maximum strain over the entire dynamic response history of the vessel, $\varepsilon_{\max}$, were taken as characteristics of the dynamic response process. It was observed by Belov, et al., that a charge shift toward the lower pole results in an increase in the (first cycle) peak strain, ε_1, at that pole location. However, changes in ε_1 in the vicinity of the equator and the top port were found to be insignificant.

Further, it was reported that the maximum strain, $\varepsilon_{\max}$, which occurs later in time, appears to be independent of charge eccentricity. It is important to note that maximum strain greatly exceeds the peak strain in the first half-cycle of vessel response. Therefore, at least up to the maximum degree of charge eccentricity considered by Belov, et al. (20%), charge eccentricity is not a significant parameter on maximum containment vessel response.

More recently, Stevens [19] performed a parameter study to evaluate the effects of varying the location of a spherical mass of high explosive detonated inside a Containment Vessel similar to that shown in Fig. 1.1, but in which the side ports were omitted. The vessel was, therefore, qualitatively similar to that of Belov, et al. [18]. Stevens [19] considered charge eccentricities up to 0.3.

Computer simulations were performed for a 40-lb high explosive charge, using ABAQUS/Explicit for the (axisymmetric) vessel structural model and CTH [18], described above, for the input pressure-time forcing functions. Stevens [19] compared maximum values of several measures of vessel response at locations near the top port, the equator, and the south pole of the vessel as a function of charge eccentricity.

Stevens [19] reported anomalous results: First, the structural responses did not vary monotonically with the HE location. Moreover, he reported that small perturbations in the HE location can cause large differences in structural response levels. However, he did find, in agreement with Belov, et al. [18], that maximum response at the equator is independent of charge eccentricity. However, at other locations, maximum strains were found to be strongly dependent upon charge eccentricity, in disagreement with Belov, et al [18].

It is concluded, based upon the studies reported, that it is difficult to draw general conclusions regarding the influence of asymmetric loading, whether from an off-center-initiated charge or from a charge placed off center in the vessel. In most cases, response (peak stress/strain) does increase for asymmetric loading, however.

4.0 EXPLOSION PHENOMENA

An explosion is a rapid self-propagating chemical decomposition followed by large releases of heat and detonation products (i.e., gases). The chemical reaction within the HE is initiated by the heat and is accompanied by shock compression. The shock wave propagates into unreacted material at supersonic speeds.

The ensuing explosion creates a shock wave within the interacting medium, air. Shock waves are compression waves in an elastic medium, which travel at supersonic speeds in air [20]. In

performing a vessel design to withstand HE detonation (blast) loading, the ultimate goal is to understand the transient forcing function to adequately assess the state-of-strain throughout the structure. Determination of shock velocities and dynamic pressures attained during a detonation phase can be accomplished in one of several ways;

(1) Theory - Theoretical application of thermochemistry and thermophysics of HE detonations, coupled with reaction products equations-of-state (EOS) solutions [20-26], are used in simplified geometry,

(2) Design Manuals - Graphical or mathematical representations of air-blast (i.e., shock-wave) parameters, based on empirical data performed for numerous high explosives [22, 24, 25],

(3) Approximate Wave Codes - Simple, fast-running, PC-based computer programs founded upon parametric equations of (1) and (2) above, provide highly reliable results for simplified geometries, and

(4) Multi-dimensional Hydrocodes - High-fidelity Eulerian hydrodynamics (i.e., shock-wave propagation) codes are employed [14,17] to obtain a high-order source-term representation of complex geometries and/or complex shock-wave interactions.

The loading functions developed from a detonation can be extremely complex. In non-symmetric geometries, wave reflections and rarefactions collide with incident waves creating a somewhat chaotic system, which simple empirical solutions cannot provide. These reflections and subsequent secondary impulses may be significant in structures that are not truly spherical. For these cases, a complete numerical hydrodynamics code simulation may be required.

However, simplified methods, coupled with symmetric geometries such as spheres and cylinders, provide valid solutions for the initial loading pulse. These simplified methods have some level of conservatism. That is, with knowledge of the peak dynamic pressure and the decaying loading function, an upper-bound estimate can be made for design purposes.

4.1 Deflagrations versus Detonations

ASME Code Section VIII, Division 1, Appendix H, "*Guidance to Accommodate Loadings Produced by Deflagrations,*" contains design criteria for pressure vessels under high-rate burning (i.e., deflagration) loading. As such, this section provides a brief discussion relative to differences between deflagrations and detonations, and thus places the phenomenon of detonations in perspective.

Deflagrations are high-rate combustion reactions (i.e., burning events), where the deflagration velocity within the mass may be between 0.05 and 500 m/s. Although a large-scale deflagration may appear to the observer as an explosion, in fact the event is measured in the milli-second (ms) to seconds (s) time frame. Detonations are described as explosions traveling at a very high and constant velocity of between 1 to 9 km/s [20], depending on the type of explosive. High explosives attain shock wave speeds between 5 km/s and 9 km/s [20]. Detonations occur within the micro-second (μs) to milli-second (ms) range. As an example, for a given mass of HE, the energy release of a detonation is an order of magnitude greater than that of a deflagration.

Detonations differ from deflagrations in two distinct manners. In deflagrations (i.e., combustion), there is an unlimited amount of oxidizer, or oxygen in surrounding air. An explosive undergoing detonation, on the other hand, oxidizes so quickly that it usually must contain its own source of oxygen. Since most high explosives are composed of C-H-N-O, carbon, hydrogen, nitrogen, and oxygen, the oxidizer is maintained within the explosive [21]. However, if there is more oxygen available, there will be an additional amount of heat generated due to combustible reaction products such as carbon (C) or carbon-monoxide (CO). Detonations and deflagrations also differ in their performance characteristics. The performance of a deflagrating fuel is evaluated in the amount of heat released, whereas the performance of a detonating explosive has a less direct relationship to heat release. A measure of the differences between deflagrations and detonations is shown in the following table:

Table 4.1 – Detonation-Deflagration Comparison [20]

Characteristic	Deflagrations	Detonations
Wave	Subsonic	Supersonic
Velocity	0.05 to 500 m/s	1000 to 9000 m/s
Power Density	1E+6 W/cm^3	1E+10 W/cm^3

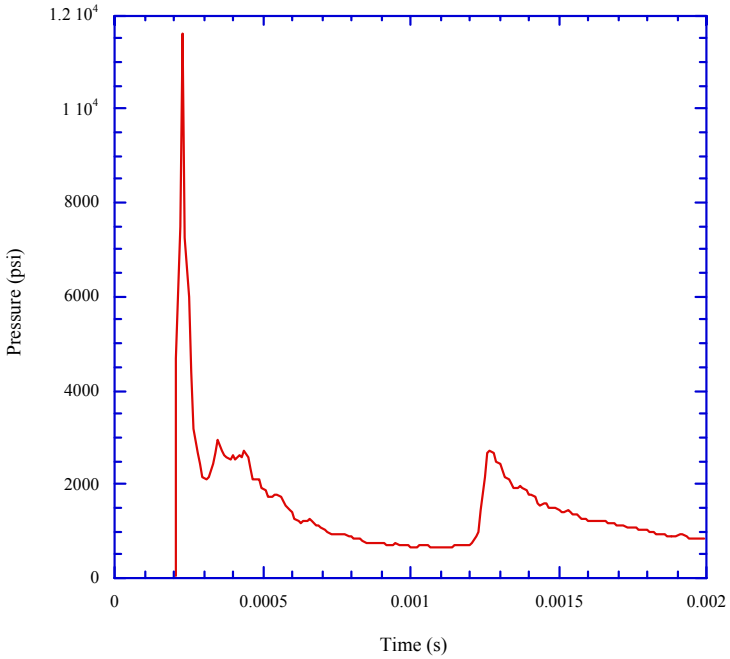

Figure 4.1. – Detonation pressure of 40-lb HE in spherical LANL vessel.

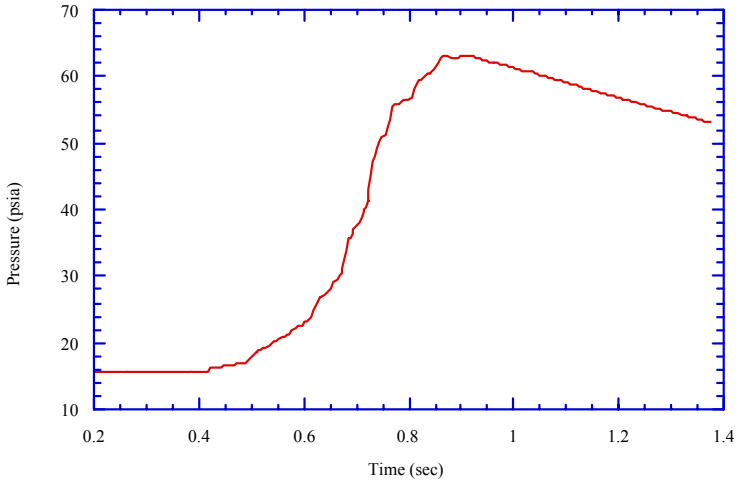

Figure 4.2. – Deflagration pressure from 13,000 ft^3 of H_2 in underground tank.

Figures 4.1 and 4.2 show a detonation and deflagration pressure-time history respectively. Of interest here is comparison of the initial source-term (i.e., loading) rate. Figure 4.1 shows a step function rising from ambient pressure to some peak value, which is indicative of a shock front. Figure 4.2 depicts a much more gradual pressure rise from ambient conditions.

As previously discussed, the important loading parameter for a *detonation* is the impulse, or the area under the pressure-time history curve. The peak value of the pressure is inconsequential. Also, the shape of the impulse curve is of no direct importance, as discussed in Section 2.4. Conversely, the important loading parameter in a *deflagration* is the peak pressure attained during the transient. Figure 4.2 represents a deflagration p(t) history from a 13,000-ft^3 volume of hydrogen in an underground tank. The rate of pressure (dP/dt) does have an amplification effect on the tank's structural response.

4.2 Detonation Physics

Detonation is a field of shock-wave physics that has been widely researched, with great advances occurring during the past century. The fundamental condition of a detonation is the creation of a shock-front that travels at speeds in excess of the sound speed. The particles (i.e., air for example) ahead of the shock-front are at ambient conditions (i.e., $P = P_o$, $\rho = \rho_o$, and $T = T_o$) while those immediately behind the shock-front are at shocked values (i.e., $P = P_1$, $\rho = \rho_1$, and $T = T_1$). The change in pressure, density, and temperature across the shock front is not gradual, nor along some gradient, but discontinuously jump from unshocked to shocked values [21]. In effect, the shocked state is a step function from ambient conditions. The fundamental relations between the unshocked and shocked states are referred to as the "Jump" equations, yet more precisely known as the Rankine-Hugoniot equations [20-23]. These are developed from the fundamental conservation equations: mass, momentum, and energy.

Mass

$$\frac{\rho_1}{\rho_0} = \frac{U - u_o}{U - u_1} \tag{4.1}$$

Momentum

$$P_1 - P_o = \rho_o (u_1 - u_o)(U - u_o) \tag{4.2}$$

Energy

$$E_1 - E_o = \frac{P_1 u_1 - P_o u_o}{\rho_o (U - u_o)} - \frac{1}{2}\left(u_1^2 - u_o^2\right) \tag{4.3}$$

where,

ρ = Density u = Particle velocity

P = Pressure U = Shock velocity

E = Specific internal energy

The subscripts (o, 1) in the above equations refer to the unshocked and shocked states respectively. There are five dependent variables and three equations, implying that an additional two relations are required to solve for shock wave characteristics.

The first required relationship is called an equation-of-state (EOS), which relates specific internal energy as a function of pressure and volume, $E = f(P,V)$. When combined with the jump energy equation, the specific internal energy term is eliminated, resulting in pressure as a function of volume relation $P = f(V)$, much like the Ideal Gas EOS relates gas expansion;

$$PV = nRT \tag{4.4}$$

However, it is not acceptable to use the Ideal Gas EOS for explosive reaction products, except in special instances. Detonation pressures and temperatures are of the order of several hundred thousand atmospheres and several thousand degrees Kelvin. A rule of thumb is that the Ideal Gas EOS, or the Nobel-Able modification to the Ideal Gas EOS, may be used when peak pressures are below 200 atmospheres and temperatures are less than 4000 degrees Kelvin.

The EOS is obtained through graphical or empirical representation of actual test data, which is commonly referred to as the "Hugoniot." The Hugoniot provides a relation between the shock velocity (U) and particle velocity (u_o), or through manipulation of the conservation equations, between shock pressure (P) and specific volume (v), i.e., reciprocal of density. A typical Hugoniot for an explosive is shown in Figure 4.3.

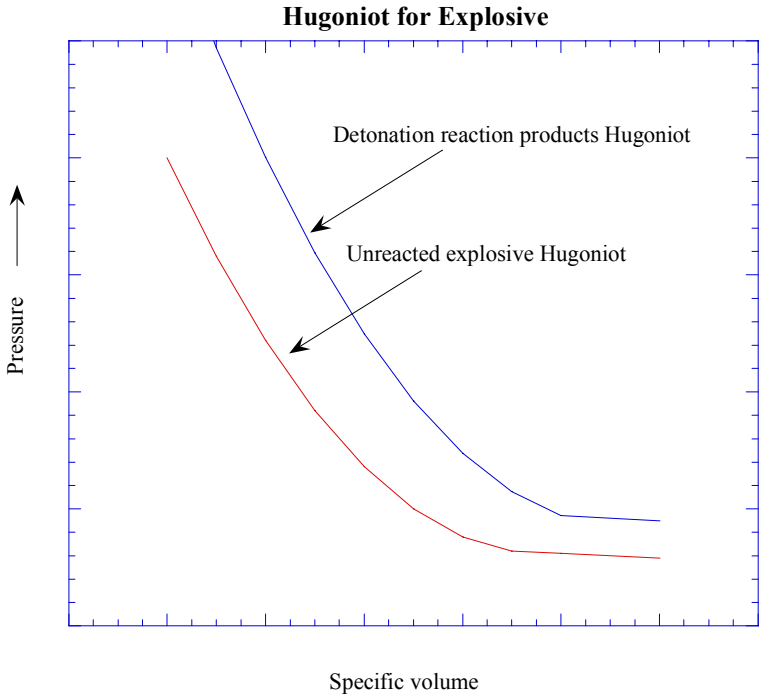

Figure 4.3. – Hugoniot for typical unreacted and reacted explosive.

For explosion reaction product gases, the most widely accepted equation-of-state is the Jones-Wilkins-Lee (JWL) EOS [20, 21, 23, 27].

$$P = Ae^{-R_1 V/V_o} + Be^{-R_2 V/V_o} + C\left(\frac{V}{V_o}\right)^{-(1+\omega)} \qquad (4.5)$$

where $A, B, C, R_1, R_2, \omega$ = JWL parameters (derived from experimental data)

V, V_o = Specific volumes; at pressure and initial states.

The final relation required to solve for the shock parameters is a value for one of the variables for a particular shock wave. A parameter well characterized by experimenters is the detonation velocity (D) of a particular explosive. The detonation velocity is related to a parameter termed the C-J (or Chapman-Jouguet) pressure. Knowing the HE detonation velocity, the "Jump" or Rankine-Hugoniot equations can now be written in terms of (D) instead of shock velocity (U).

4.3 Transient Pressure Calculations

Design manuals (e.g., TM 5-1300 [24] and DOE/TIC-11268 [25]) used to design structures to resist the effects of accidental explosions have been based on principles of shock physics whereby the transient shock pressure is determined over the structure. In addition, highly specialized and sophisticated hydrodynamic numerical codes, or hydrocodes, (e.g., MESA-2D [14], CTH [17], and AUTODYN [28]) exist for detailed and refined calculations of transient pressure loadings on structures.

4.3.1 TM 5-1300 and DOE/TIC-11268 Philosophy

US Army, Navy, and Air Force manuals were developed to assist in design of protective structures to resist the effect of conventional weapons. TM 5-1300 [24] provides graphical shock wave parameters for HE detonations. These parameters have been calibrated in the field for numerous explosives and conditions.

As previously mentioned, the loading functions developed from a detonation can be extremely complex. These loading functions can be obtained from both hydrodynamic numerical simulations (e.g., MESA-2D [14], CTH [17], or AUTODYN [28]) or design manuals created specifically for the U.S. Department of Defense (DoD) and Department of Energy (DOE). One such manual, typically referred to as TM 5-1300 [24] is commonly used by structural designers for blast protection design. Another manual, DOE/TIC-11268 [25], is also used for blast protection design and is based on the information provided in TM 5-1300. Both these manuals present methods of design for protective construction used in facilities for development, testing, production, storage, maintenance, modification, inspection, demilitarization, and disposal of explosive materials [25].

These design manuals are considered industry standards for blast resistant design. They facilitate the determination of blast loads but do lack the sophistication and refinement offered by hydrodynamic numerical simulations. Another excellent source for high explosion blast design is Baker [22]. Unfortunately, these design manuals do not provide guidance on the detailed response of internal blast containment structures at discontinuities such as door frames, flanges, changes of section and junctions between walls and roofs. As such, the use of 2D/3D hydrocode and structural Finite Element models are required in these cases to assess the true state of strain at these locations as well as throughout the remainder of the vessel.

This section will focus on how to use these design manuals to determine the pressure-time loading functions for *spherical* containment vessels from a bare, spherical, center initiated high explosive detonation. The fundamental concepts of TNT-Equivalence, Blast Wave Structure, Blast Categories, and Scaled Distance will be discussed. For explosive/vessel geometries lacking spherical symmetry, subsequent reflections and secondary impulses may be important, indicating the need for more refined hydrodynamic calculations.

4.3.1.1 TNT-Equivalence

When explosion sources consist of highly explosive (HE) solids or liquids, or similar energetic materials, all will generate blast waves, which are similar in nature. The strengths and durations of the blast waves will differ because of the explosive materials and their associated densities, and heats of detonation and combustion [25]. There exists a significant amount of measured blast data for TNT explosive. An approximate conversion for other explosives to an equivalent weight or mass of TNT can be determined. This is referred to as "TNT-Equivalence" and is defined as:

$$W_{TNT} = \frac{H^{d}_{Exp}}{H^{d}_{TNT}} W_{Exp} \qquad (4.6)$$

where: W_{TNT} = TNT-Equivalent HE Weight

W_{Exp} = Weight of HE charge in question

H^{d}_{Exp} = Heat of Detonation of HE in question

H^{d}_{TNT} = Heat of Detonation of TNT

TNT-Equivalence is required to determine the air blast parameters of a high explosive detonation using TM 5-1300 or DOE/TIC-11268 design manuals.

4.3.1.2 Air Blast Wave Structure

In explosions involving HE, blast waves from both single and multiple sources with bare or cased HE charges may exist. For this discussion, only single source HE explosions from bare, spherical, center initiated HE charges will be considered. References [24] and [25] contain details on multiple source explosions and cased HE charges. Figure 4.4 shows an ideal HE air blast wave structure. As the blast wave expands, it decays in strength, lengthens in duration, and slows down, both because of spherical divergence and because the chemical reaction is over, except for afterburning, as the hot explosion products mix with the surrounding air [25].

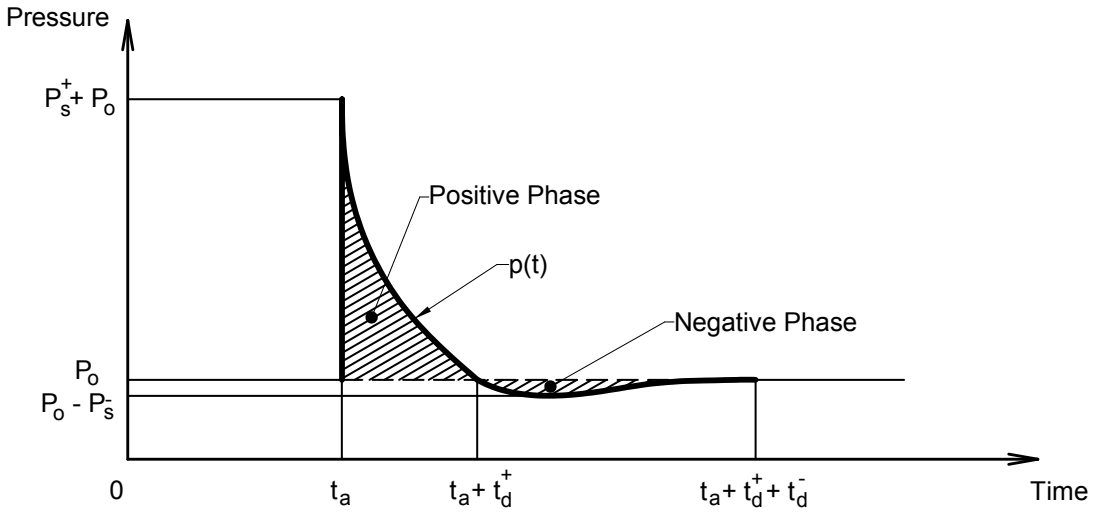

Figure 4.4. - Ideal Blast Wave Structure

The blast parameters shown in Figure 4.4 are defined as:

P_o = Ambient Pressure

P_s^+ = Positive Peak Overpressure (Positive Phase of Blast Wave)

P_s^- = Partial Vacuum (Negative Phase of Blast Wave)

t_a = Arrival Time of Blast Wave to Structure

t_d^+ = Duration of Positive Phase Blast Wave

t_d^- = Duration of Negative Phase Blast Wave

$p(t) =$ Pressure-Time History of Blast Wave

The crosshatched areas in Figure 4.4 identify both the positive and negative impulses, I_s^+ and I_s^-. In most blast studies, the negative phase of the blast wave is ignored because $P_s^+ >> P_s^-$ and $I_s^+ >> I_s^-$ and only the blast parameters associated with the positive phase are considered.

4.3.1.3 Blast Loading Categories

TM 5-1300 shows that blast loads on structures can be divided into two main groups based on the confinement of the explosive charge (unconfined and confined explosions) and can be subdivided based on the blast loading produced. Free-air burst (internal shock) blast parameters from TM 5-1300 for a fully confined structure (internal gas) can be use for many blast-loaded containment vessel designs (e.g., spherical vessels and cylindrical vessels with a length-to-diameter ratio near one).

A free-air burst explosion occurs in free air, producing an initial output whose shock wave propagates away from the center of the detonation, striking the protective structure without intermediate amplification of its wave. Additionally, full confinement of an explosion is associated with either total or near total containment of the explosion. Internal blast loads will therefore consist of unvented shock loads and very long duration gas pressures, which are a function of the degree of containment.

4.3.1.4 Scaled Distance

Blast curves in TM 5-1300 are plotted in terms of scaled distance from the HE charge to the structure,

$$Z = \frac{R}{W^{1/3}} \tag{4.7}$$

where: $Z =$ Scaled Distance (ft/lb$^{1/3}$)

$R =$ Distance to Structure from Center of High Explosive (ft)

$W^{1/3} =$ Weight of TNT Equivalent HE (lb$^{1/3}$)

4.3.1.5 Determining Pressure-Time History

Pressure-time loadings from a high explosive detonation within a containment vessel can now be determined by utilizing the fundamental concepts of TNT-Equivalence, Blast Wave Structure, Blast Load Categories, and Scaled Distance.

It should be noted that the blast data provided in TM 5-1300 primarily relate to bare, spherical, center initiated HE detonations. Methods do exist, however, to account for different HE geometries and casings. Additionally, data are provided only for the first peak overpressure and associated impulse. Subsequent shock wave reflections (i.e., reverberations) from the inner surface of containment vessels after the detonation are typically neglected because of their smaller scale relative to the initial pressure pulse. Hydrodynamic numerical simulations could be used to capture these shock wave reflections and details of the blast wave for more refined calculations. Moreover, DOE/TIC-11268 presents a simplified method to account for these shock wave reflections using a scaling factor for the initial peak overpressure.

As indicated above, fully confined explosions, typical in blast containment vessel design, exhibit both an initial shock wave (i.e., impulse load) and a long-term quasi-static overpressure (residual, quasi-static pressure load). TM 5-1300 provides methods for determining both these loading conditions using empirical data obtained from many DoD and DOE experiments. Figure 4.5 (Free Air Burst Blast Parameters) and Figure 4.6 (Maximum Gas Pressure - Residual Pressure) are two sets of curves obtained from TM 5-1300 that can be used to determine pressure loadings in blast-loaded containment vessels.

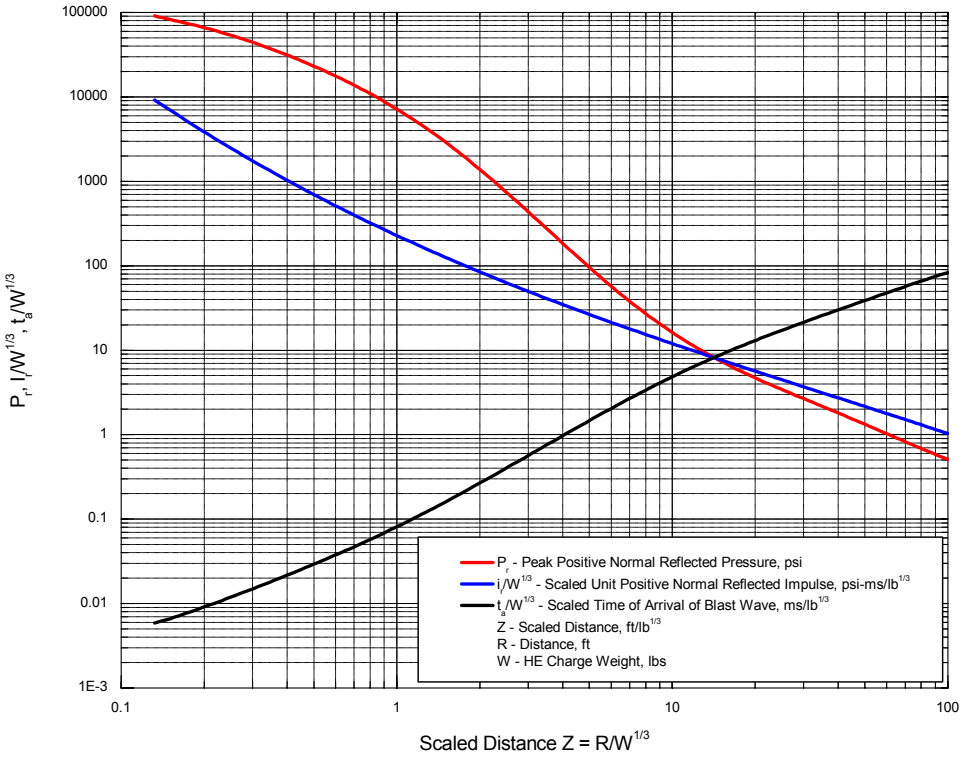

Figure 4.5. - Positive Phase Shock Wave Parameters for a Free-Air Burst

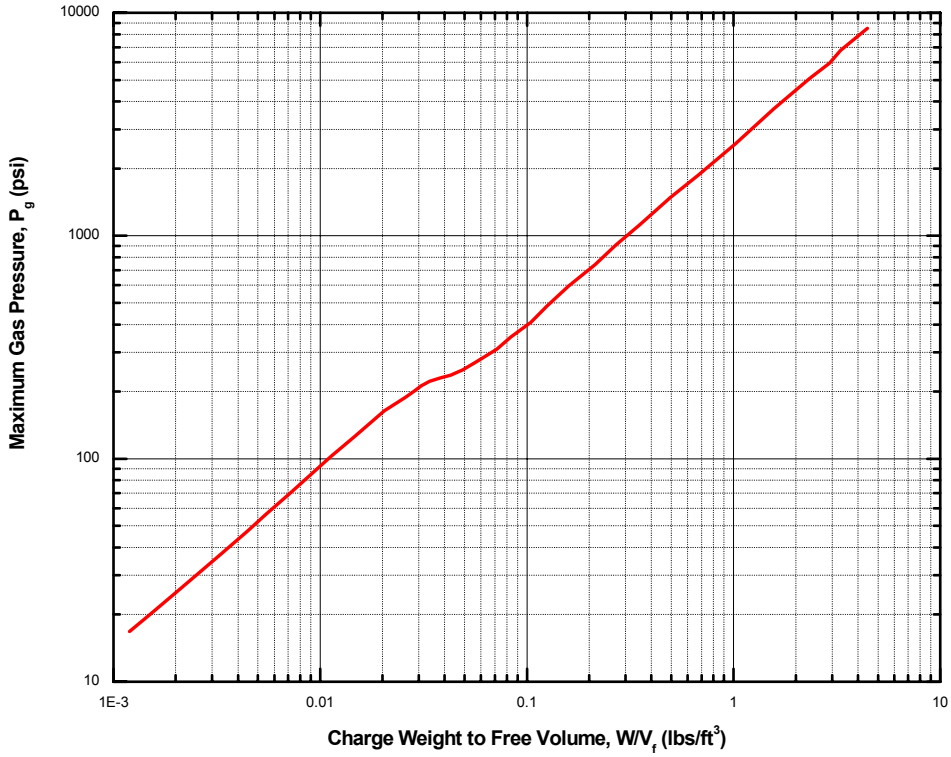

Figure 4.6. - Peak Gas Pressure Produced by a TNT Detonation in a Contained Chamber

The following information is used to obtain the blast parameters provided in TM 5-1300 or DOE/TIC-11268:

- HE Type
- HE Weight
- Distance from the HE Center to the Structure

Given this information, the following procedure for obtaining the blast data can then be used:

- The HE Weight is converted to a TNT-Equivalent Weight
- Per TM 5-1300 guidance, the TNT-Equivalent Weight is increased by 20% to account for manufacturing and construction uncertainties of the HE and Structure
- The Scaled Distance, Z, is determined knowing the Distance to the Structure and TNT-Equivalent Weight

- Figure 4.5 is then used to obtain the following blast parameters knowing the value of the Scaled Distance, Z:

  $P_r =$ Peak Positive Normal-Reflected Pressure, psi

  $\frac{I_r}{W^{1/3}} =$ Scaled Unit Positive Normal Reflected Impulse, psi-ms/lb$^{1/3}$

  $\frac{t_a}{W^{1/3}} =$ Scaled Time of Arrival of Blast Wave, ms/lb$^{1/3}$

- The load duration, t_d is determined knowing I_r and P_r and by assuming a simple triangular pulse, or

$$t_d = \frac{2I_r}{P_r}$$

- The Internal Free Volume, V_f, of the containment vessel is determined to obtain the residual quasi-static pressure
- The ratio of TNT-Equivalent Weight to Internal Free Volume is determined
- Residual pressure, P_{Residual}, is then obtained from Figure 4.6
- The pressure-time history is determined as shown in Figure 4.7

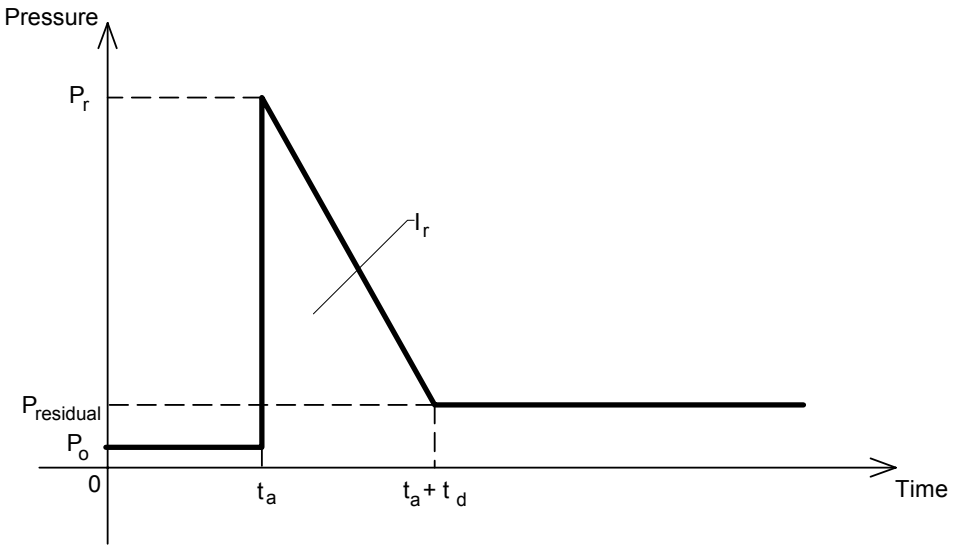

Figure 4.7. - Pressure-Time History using TM 5-1300 Blast Data

4.3.2 Numerical Hydrodynamics Codes

Hydrodynamics codes, or hydrocodes, are the most commonly used, robust, and efficient tools for determining transient pressures due to detonations in complex geometries with complex shock interactions. The majority of hydrocodes are Eulerian, incorporating multi-material, multi-physics, second-order accurate, explicit finite difference schemes. The two codes used in determination of transient pressures for this study are MESA-2D [14] and CTH [17]. Another code, which is commercially available, is AUTODYN [28]. For brevity, only a discussion of CTH is provided.

CTH is a family of codes developed at Sandia National Laboratories (SNL) for modeling complex multi-dimensional, multi-material problems that are characterized by large deformations and/or strong shocks. A two-step, second-order accurate Eulerian solution algorithm is used to solve the mass, momentum, and energy conservation equations. CTH includes models for material strength, fracture, porous materials, and high-explosive detonation and initiation, as well as viscoplastic or rate-dependent models of material strength. The strength formulations of Johnson-Cook, Zerilli-Armstrong, and Steinberg-Guinan-Lund are standard options within CTH. The advancements made in modeling material response have significantly improved the ability of CTH to model complex large-deformation, plastic-flow dominated phenomena.

Hydrodynamic codes, as the name implies, are based on the fundamental equations of fluid mechanics; conservation of mass, momentum, and energy. The fluid medium is, of course, continuously deformable, has very little cohesion between particles, and may be compressible or incompressible [27]. In the study of high-velocity penetration mechanics, the projectile and target interface is considered a fluid medium because impact stresses are of the order of 30-50 kbars (400,000 to 700,000 psi). Material strength is no longer significant at these extremely high pressures. That is, the material under these high pressures "flows" much like a fluid.

The detonation of energetic material under shock loading conditions has been an area of great interest. A recently developed model of reactive burn for high explosives (HE) has been added to CTH. This model along with tabular equations-of-state for the HE reaction by-products has been compared to one- and two-dimensional explosive detonation experiments. These comparisons indicate excellent agreement of CTH predictions with experimental results. A reactive burn model coupled with advances in equation-of-state modeling make it possible to predict multi-dimensional burn phenomena without modifying model parameters for different dimensionality. This implementation is significant because it represents the first time a multi-dimensional model has been used to successfully predict multi-dimensional detonation effects without requiring a modification of the model parameters.

Figure 4.8 shows a typical cylindrical pressure vessel with hemispherical end-caps undergoing a detonation event, modeled in 2-D cylindrical system. HE is placed at the center of the model, with detonation initiation beginning at time t=0. The figure shows pressure gradients from the HE reaction products at 200 μs .

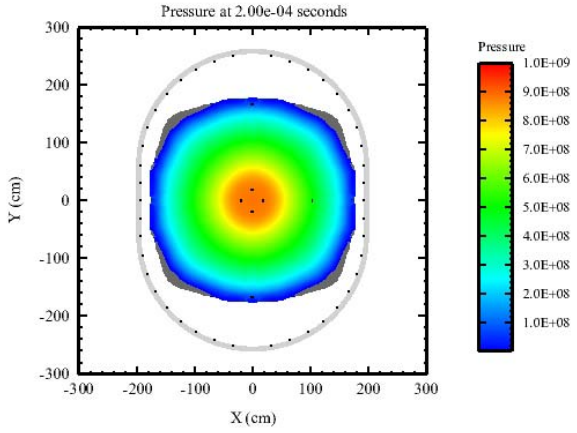

Figure 4.8. – Pressure contours of internal vessel detonation @ 200 μs .

Figure 4.9 shows pressure contours for the same vessel (i.e., geometry) as Figure 4.8, but at 2.5 ms into the transient. It is evident from Figure 4.9 that full mixing of the reaction products has occurred and small-scale rarefaction waves are still impacting the vessel wall. The shape of the actual pressure-time history looks much like that of Figure 4.1. The secondary pressure pulses apply little additional energy to the system, and the initial pressure pulse (i.e., initial impulse) provides the primary driving energy to the system.

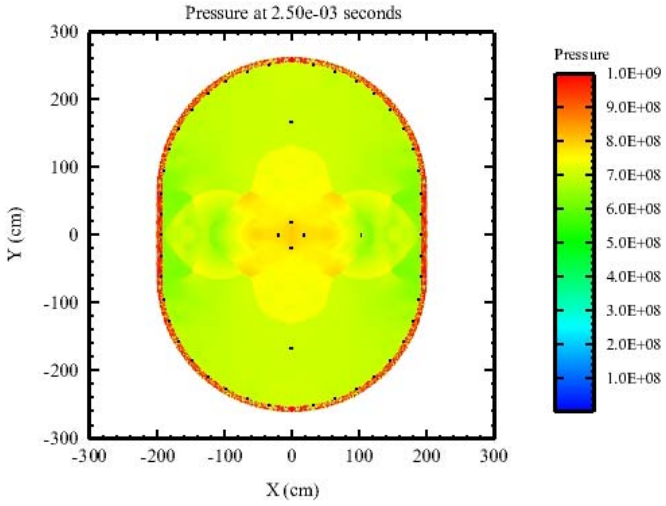

Figure 4.9. – Pressure contours @ 2500 μs (2.5 ms).

Figures 4.10 and 4.11 show a 3D model of a spherical end-cap in a cylindrical vessel with a nozzle connection. A detonation is initiated in the spherical portion of the vessel with shock waves traveling towards the nozzle region.

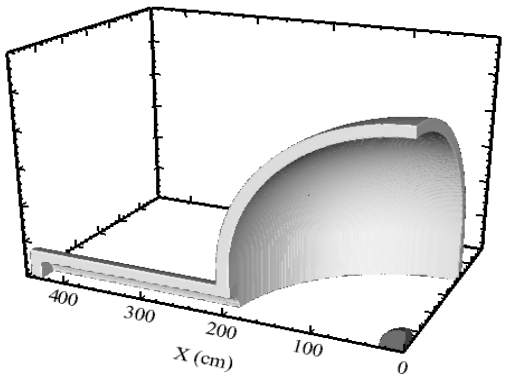

Figure 4.10. – 3D Model of HE detonation in spherical vessel with nozzle.

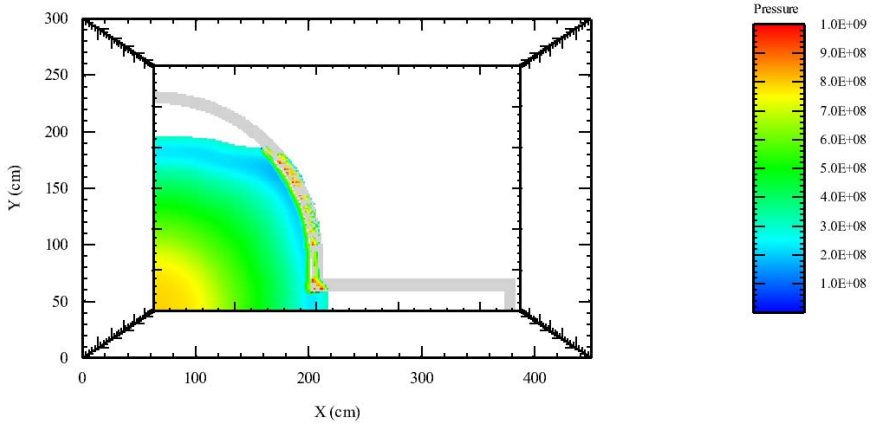

Figure 4.11. – Pressure contour results for 3D model.

The models shown above are tremendously complex and can only be solved with hydrodynamic numerical codes. The simplified approaches of section 4.3 will provide some insight as to the potential peak pressures but will not be accurate enough to detail the impulse on the complete system.

5.0 VIBRATION MODES OF SPHERICAL SHELLS AND CONTAINMENT VESSELS

In this Section, the vibrations of a spherical containment vessel are investigated for vessel response in the elastic range. These vibration modes, and particularly the spacing of natural frequencies, have recently been shown to be the mechanism of the 'strain growth' phenomenon [29]. 'Strain growth' is a phenomenon in which the maximum vessel response amplitude occurs later in time, i.e., well beyond the first response peak and in which the strain amplitude oscillates with time over an extended period (amplitude modulation caused by modal beating effects).

A typical spherical containment vessel, with nozzles, is shown in Fig. 1.1. Vibrations of such a containment vessel are related to those of a complete spherical shell. Therefore, a review of the literature on vibrations of a complete spherical shell is first presented in the next Subsection (5.1), followed by a comparison of natural frequencies of axisymmetric (Subsection 5.2) and nonaxisymmetric (Subsection 5.3) modes of a complete spherical shell with ABAQUS finite element predictions. Corresponding natural frequencies of the more complex, spherical

containment vessel are also compared in Subsection 5.3. Limited frequency comparisons with experimental results are presented in Subsection 5.4, followed by a summary section.

5.1 Literature Survey

Baker [30] extended the early work of H. Lamb [31] to determine the axisymmetric vibration modes of a thin complete spherical shell. He utilized a membrane shell theory and observed two types of vibration mode sets, falling on a lower and an upper branch. The lower branch was found to consist of an infinite number of modes, spaced within a finite frequency interval. Baker also demonstrated by experiment that the two types of vibration modes do in fact exist.

Silbiger [32] presented a brief discussion of the presence of nonaxisymmetric modes of spherical shells, using Baker's [30] two-branch, membrane solution as a basis. Silbiger states that nonaxisymmetric modes do indeed exist and that the corresponding frequencies are identical to the frequencies of the axisymmetric modes. He goes on to state that, for each branch, one can select only 2n+1 linearly independent nonaxisymmetric modes, all other modes being linear combinations of the 2n+1 modes.

Kalnins [33] again examined axisymmetric modes of a complete spherical shell, but included the effects of bending. He also found that the frequency spectrum consists of two infinite sets of modes. He labeled one branch as flexural and the other as membrane, the distinction made on the basis of the comparison of strain energies due to bending and stretching of each mode[1]. However, he observed a fundamental difference in the lower branch behavior, as compared to Baker [30], due to the inclusion of bending. He showed that the lower branch modes are a degenerate case of bending modes in the membrane theory, applicable only to zero thickness shells. When Kalnins introduced the bending theory, the frequency interval for this lower branch was found to extend to infinity for every non-zero thickness shell (rather than all modes being spaced within a finite interval of the frequency spectrum). The upper (membrane) branch was nominally identical to that of Baker.

Niordson [34] rederived the equations for bending vibrations of a spherical shell in a somewhat different form. He examined the nonaxisymmetric modes as well, concluding that there exist n+1

(not 2n+1 as reported by Silbiger) modes at each frequency on each branch. Observations in [34] made regarding nonaxisymmetric modes (e.g., the fact that they exhibit the frequency degeneracy identified by Silbiger [32]) were similar, except for the number of independent modes anticipated.

Wilkinson [35] again investigated axisymmetric modes of a complete spherical shell, but with the effects of transverse shear and rotatory inertia included. Not surprisingly, he observed a third branch at higher frequencies because of the inclusion of shear deformations.

Shah, et al. [36] investigated nonaxisymmetric wave propagation in a hollow elastic sphere. They presented a shell theory in which the effects of transverse normal strain are included as are transverse shear and rotary inertia. This represents a progressive extension of earlier work cited above. Shah, et al., observed the presence of axisymmetric modes which are independent of the circumferential angle. They then state that, by a suitable superposition of the axisymmetric modes of vibration about different axes, but of identical natural frequency, a nonaxisymmetric vibration mode of the same frequency results, in agreement with observations made by Silbiger [32] and Niordson [34].

Hirai and Kuroda [37] investigated the natural vibrations of a spherical shell of variable thickness in the meridional direction. They investigated nonaxisymmetrical vibrations. Unfortunately, results were only presented for a hemispherical shell. Furthermore, no general information regarding the role played by nonaxisymmetrical modes was given.

Evans [38] investigates nonaxisymmetric modes of a complete spherical shell, placing his results in terms of modal impedances. The work is limited to extensional effects for a thin shell, i.e., membrane theory only. Evans claims that Silbiger [32] overlooked the fact that there is a lack of orthogonality of certain of the nonaxisymmetric modes. Evans does, however, confirm Silbiger's observation that natural frequencies of nonaxisymmetric modes agree with their axisymmetric mode counterparts, i.e., that natural frequencies of the nonaxisymmetric modes are degenerate.

Useful numerical results on the vibration of complete spherical shells are presented in the ABAQUS/Standard Example Problems Manual [39]. Both axisymmetric and nonaxisymmetric

[1] A closed shell cannot undergo pure bending. A mode is either purely extensional (membrane) or combined bending-extensional, but can (on an energy basis) be "mostly" bending. Stated another way, no modes will be present for which the extension

comparisons are presented. For nonaxisymmetric modes, the first 20 eigenvalues were investigated. Indeed, as predicted by Silbiger [32], 2n+1 linearly independent modes were recovered corresponding to each value of n investigated.

5.2 Axisymmetric Modes of Vibration

Axisymmetric modes are independent of the circumferential angle, θ (See Fig. 5.1). A detailed discussion of axisymmetric *membrane* modes of a complete spherical shell is presented in [30]. Modes of vibration are expressed in terms of Legendre Polynomials of integer indices, n. For each value of $n \geq 2$, there are two branches, i.e., two separate, but similar, mode shapes, and two distinct frequencies (For n = 0, there is only one real root, corresponding to the 'fundamental' membrane or 'breathing' mode; n = 1 corresponds to purely rigid-body displacement, i.e., no distortions). The lower branch approaches an asymptotic value for large n, as described in [30], which unfortunately appears to be physically meaningless because the intervals between the natural frequencies apparently become increasingly small [33].

The elementary bending/membrane theory developed in [33] has a similar upper branch when compared against the membrane theory. However, the lower branch monotonically increases with integer index number when bending is included. Natural frequencies for these axisymmetric bending/membrane modes are plotted as a function of index number in Figure 5.2

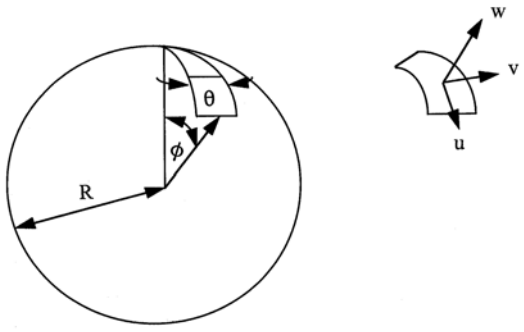

Figure 5.1 Complete Spherical Shell

of the middle surface is identically zero.

using the following geometry and material parameters relevant to the example spherical Containment Vessel introduced earlier in the Report:

Shell thickness h=2.00 in
Mean radius R=37.0 in
Elastic modulus $E=29.9 \times 10^{6}$ psi
Mass density $\mu=7.32 \times 10^{-4}$ lbf-sec^2/in^4
Poisson's ratio $\nu=0.29$

The upper and lower branches can be clearly seen in Fig. 5.2.

In the higher-order theory [35], which includes transverse shear and rotary inertia, a third, highest branch appears, associated with the shear-deformation degree of freedom introduced. However, this highest branch is of little interest here because the frequencies are so high. The lower and upper branches nominally agree with the elementary bending/membrane theory. Therefore, attention is given to the lower and upper branches in this paper.

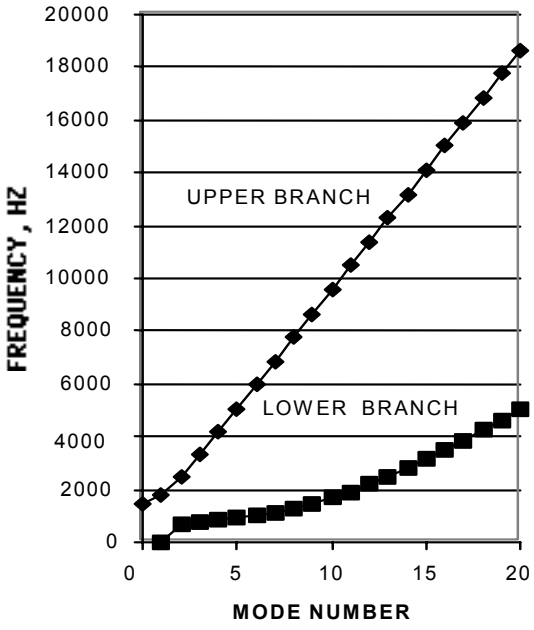

Figure 5.2 Frequencies of a Complete Spherical Shell

A finite element model of a complete spherical shell using 2-D solid axisymmetric elements was developed for use with ABAQUS, using the above shell parameters. The axisymmetric FE model consisted of a total of 2,400 elements. The first 26 modes extracted by ABAQUS are compared with the lowest 26 modes predicted by the higher-order theory of Wilkinson [35] in Table 5.1, from which the following observations can be made:

1. The first 26 modes (in ascending numerical order) draw from both lower and upper branches.

2. The lowest mode (zero frequency) is the rigid-body mode, associated with the lower branch.

3. The so-called 'fundamental' mode is actually the tenth mode to appear. It is, however, the first mode of the upper branch.

4. The percent difference in respective theoretical and ABAQUS-predicted frequencies is extremely small, in all cases much less than one percent.

5. Some of the frequencies are very close in value. For example, modes 9 and 10 have frequencies within 1 Hz, owing to the fact that the modes are associated with different branches. Modes 15 and 16 and modes 25 and 26 are also quite close. The implication is that beating effects could occur, resulting in the "strain growth" phenomenon [29]. Such effects were observed in experiments on complete spherical shells reported by Baker [30] and are the subject of a recent investigation by Whenhui, et al. [29].

TABLE 5.1
NATURAL FREQUENCY COMPARISON - AXISYMMETRIC MODES

MODE	ABAQUS	THEOR.	INDEX, n	BRANCH	PCT. DIFF.
1	1.32E-4	0.0	1 (Rigid Body)	Lower	---
2	642.77	642.84	2	Lower	0.011
3	768.69	769.36	3	Lower	0.087
4	837.87	839.39	4	Lower	0.181
5	906.61	909.33	5	Lower	0.299
6	995.67	999.55	6	Lower	0.388
7	1114.5	1119.6	7	Lower	0.456
8	1266.6	1273.3	8	Lower	0.526
9	1451.8	1459.8	9	Lower	0.548
10	1461.3	1460.7	0 (Fundamental)	Upper	0.041
11	1668.2	1676.2	10	Lower	0.477
12	1787.9	1787.2	1	Upper	0.039
13	1913.3	1921.8	11	Lower	0.442
14	2184.3	2192.8	12	Lower	0.388
15	2466.4	2467.5	2	Upper	0.045
16	2478.9	2487.5	13	Lower	0.346
17	2794.8	2802.2	14	Lower	0.264
18	3130.2	3136.9	15	Lower	0.214
19	3296.0	3297.9	3	Upper	0.058
20	3483.4	3488.0	16	Lower	0.132
21	3852.7	3855.4	17	Lower	0.070
22	4169.1	4172.8	4	Upper	0.089
23	4236.9	4237.4	18	Lower	0.012
24	4634.7	4632.1	19	Lower	0.056
25	5045.1	5038.7	20	Lower	0.127
26	5057.1	5062.3	5	Upper	0.103

5.3 Non-axisymmetric Modes of Vibration

As discussed primarily in [3.2], nonaxisymmetric modes for a complete spherical shell do exist. Nonaxisymmetric modes depend upon both θ and ϕ (See Fig. 5.1). They are degenerate: frequencies are identical to corresponding frequencies of axisymmetric modes. Silbiger [32] attributes this to the spherical symmetry of the shell. He argues that the axisymmetric modes are defined with respect to a specific set of axes. Due to the symmetry of the shell, however, it can vibrate in similar modes with a different axis orientation. For a given set of 'identical' modes (differing only in orientation), the modes will each have the same natural frequency. These axisymmetric modes of identical natural frequency can be superimposed to obtain new

nonaxisymmetric modes that have the same natural frequency as the corresponding axisymmetric mode, but which are not symmetric with respect to any axis. Silbiger [32] goes on to state that, corresponding to each natural frequency, there exist 2n+1 linearly independent modes, all other modes (at that frequency) being linear combinations of these modes. As discussed earlier, Niordson [34], apparently unaware of the work of Silbiger, predicted that for each integer n>1, there is one axisymmetric mode and n nonaxisymmetric modes, leading to n+1 (rather than 2n+1) modes at the same natural frequency. His physical explanation of the degeneracy was, however, similar to that of Silbiger.

Actual spherical containment vessels contain deviations from spherical symmetry due to the presence of nozzles, not to mention significant manufacturing variations. Silbiger [32] points out that when such a deviation from spherical symmetry occurs, the above degeneracy is no longer present, and the particular modal frequency for generic integer index, n, on one of the solution branches will split into 2n+1 distinct frequencies. In a later paper, Niordson [40] similarly indicates that when spherical symmetry of a complete spherical shell is lost, the previously degenerate frequencies form into bands, with the bandwidth related to the degree of spherical asymmetry.

Two additional models were constructed and run on ABAQUS/Standard using the geometric and material properties given in the previous section. The first was a full model of a complete spherical shell. The model utilized a total of 5,576 four-node shell elements. The second model was a full representation of the spherical containment vessel, including ports. The FE model utilized a total of 32,612 four-node shell elements. The expectation was that additional nonaxisymmetric modes would appear in both these cases, as the axisymmetric restriction of the spherical shell described in the previous section had been removed. A total of 200 normal modes of vibration were extracted using ABAQUS. Results for a limited number of selected modes are shown in Table 5.2. Contents of the eight columns of Table 5.2 are as follow:

Col. 1: This is the number of the mode extracted, in order of increasing frequency (This is not the integer index, n).

Col. 2: This is the frequency (in Hz) predicted from the appropriate axisymmetric solution [9]. In addition, because of the relaxation of the axisymmetric boundary conditions, torsional modes can occur. These torsional modes were determined from

[41]. Note further in Col. 2 that there are sets of "duplicate" frequencies, as predicted by Silbiger [32]. These correspond to the 2n+1 linearly independent nonaxisymmetric modes expected for each value of the integer index, n, for each branch.

Col.3: This is the appropriate value of the integer index, n, for the frequency value listed. This index was identified by comparing the ABAQUS-extracted frequency value of interest with predictions of the various branches of the bending-extensional (radial-tangential) modes given by Wilkinson [35] or the torsional modes [41]. Note that, in some cases for the particular geometry and material properties considered, frequencies of different modes overlap and there is some question of precise identification of the type, branch, and integer index value, n. While the precise identification of each mode does not appear essential here, what is significant is that modes in some cases are extremely closely spaced, possibly leading to a beating phenomenon and amplification of sub-harmonics.

Col 4: This column identifies the applicable branch of the observed modes.

Col. 5: This column gives the expected number of linearly independent modes, 2n+1, as predicted by Silbiger [32].

Col. 6: These are the ABAQUS-extracted normal-mode frequencies.

Col. 7: This column lists the number of observed modes from ABAQUS. A comparison of columns 5 and 7 indicates that the number of modes extracted by ABAQUS agrees precisely with the number of theoretical nonaxisymmetric modes. Examination of corresponding theoretical axisymmetric frequency values (Col. 2) with ABAQUS-calculated values indicates that agreement is excellent, at least for the lower values of n shown.

Col. 8: This column contains corresponding nonaxisymmetric ABAQUS modal extraction results for the full vessel model (including nozzles). Frequencies are seen to be somewhat similar to the nonaxisymmetric shell results, although because of the true asymmetry in the model caused primarily by the presence of the nozzles, each mode has a distinct frequency. This is precisely the behavior predicted by Silbiger

[32]: He predicted that the degeneracy would be removed, and 2n+1 distinct frequencies for each integer index, n, would appear for each branch.

TABLE 5.2
SELECTED NONAXISYMMETRIC COMPARISONS

MODE	REF. [35],[41]	INDEX (n)	BRANCH	EXPECTED NUMBER	ABAQUS FULL	OBSERVED NUMBER	VESSEL
1-3	0	1 (RB)	Lower	3 Modes	0	3 Modes	0
4-6	0	1 (RB)	Torsion	3 Modes	0	3 Modes	0
7	642.84	2	Lower		643.39		541.95
8	642.84	2	Lower		643.40		586.41
9	642.84	2	Lower		643.41		605.16
10	642.84	2	Lower		643.47		606.99
11	642.84	2	Lower		643.48		635.29
				5 Modes		5 Modes	
12	769.36	3	Lower		770.23		663.81
13	769.36	3	Lower		770.24		701.76
14	769.36	3	Lower		770.27		712.79
15	769.36	3	Lower		770.49		723.1
16	769.36	3	Lower		770.64		736.04
17	769.36	3	Lower		770.92		750.25
18	769.36	3	Lower		771.10		758.81
				7 Modes		7 Modes	
89	1460.7	0	Upper	1 Mode	1462.8	1 Mode	1421.5
137	1787.2	1	Upper		1791.6		1818.0
138	1787.2	1	Upper		1792.0		1865.6
139	1787.2	1	Upper		1792.2		1891.3
				3 Modes		3 Modes	

A comparison of spherical natural frequencies with the spherical containment vessel (with nozzles) for the first 200 modes is shown in Fig. 5.3.

As an illustration of axisymmetric and non-axisymmetric vibration mode shapes for the complete spherical shell, the set of modes 12-18 listed in Table 5.2 are shown in Fig. 5.4. Mode shapes have been amplified for visualization purposes. It is seen in Fig. 5.4 that corresponding to the mode index, n, of 3, there are 2n+1=7 distinct modes. As indicated in Table 5.2, these modes have nominally the same frequency. The mode shapes shown in Fig. 5.4 are the axisymmetric mode

and six degenerate non-axisymmetric modes. However, it is interesting to note that the degenerate modes are seen in Fig. 5.4 to occur in pairs, with each mode shape of a given pair differing only in a 90-deg. rigid-body rotation about the polar axis. If this rotation is ignored, then there are n+1 distinct modes, in agreement with Niordson [34].

5.4 Experimental Observations

The existence of 'lower branch' modes for dynamically loaded spherical vessels was first reported by Baker [30]. Both lower- and upper-branch participating modes were also reported in [42] on a vessel similar to that investigated herein. The two dominant (participating) modes were found to be the fundamental membrane mode (1397 Hz) and a lower branch mode at approximately 1100 Hz, based upon an FFT of a single strain-time record taken on the vessel outer surface. Moreover, Martineau [43] also performed an FFT of strain-time data recorded during the dynamic (High Explosive) response process on the outer surface of the vessel analyzed in this paper. He found several participating modes, as shown in Table 5.3. Comparisons with modal frequencies from ABAQUS calculations are also indicated in Table 5.3. Note that, with the exception of the 'fundamental' mode the precise identification of the participating mode in Table 3 is not necessarily assured in view of finite-element modeling approximations taken, including the neglect of the rather significant spatial variation in the vessel thickness due to the manufacturing process. It is clear, however, that modes from both lower and upper branches significantly participate in the transient vessel response, with several participating modes below the so-called 'fundamental' mode.

TABLE 5.3
A COMPARISON OF OBSERVED PARTICIPATING MODES

EXPERIMENTAL FREQUENCY, HZ	ESTIMATED BRANCH	ESTIMATED MODE NUMBER, N
836	Lower	5
936	Lower	6
1025	Lower	Unknown
1169	Lower	7
1357	Upper	0 'Fundamental'
1556	Lower or Upper	Unknown

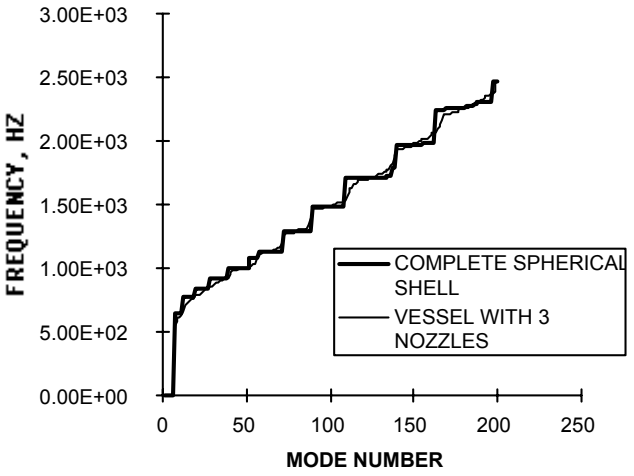

Figure 5.3 Frequency Comparison for Complete Spherical Shell Model and Spherical Containment Vessel

5.5 Summary of Containment Vessel Vibrations

Vibration modes of containment vessels are of particular interest, as it is the superposition and interaction of different modes of response with closely spaced frequencies that has been reported in the literature to be the mechanism of late-time 'strain growth' in these vessels. Figure 5.4 shows a representation of a spherical vessel vibration modes for the n=3 lower-branch.

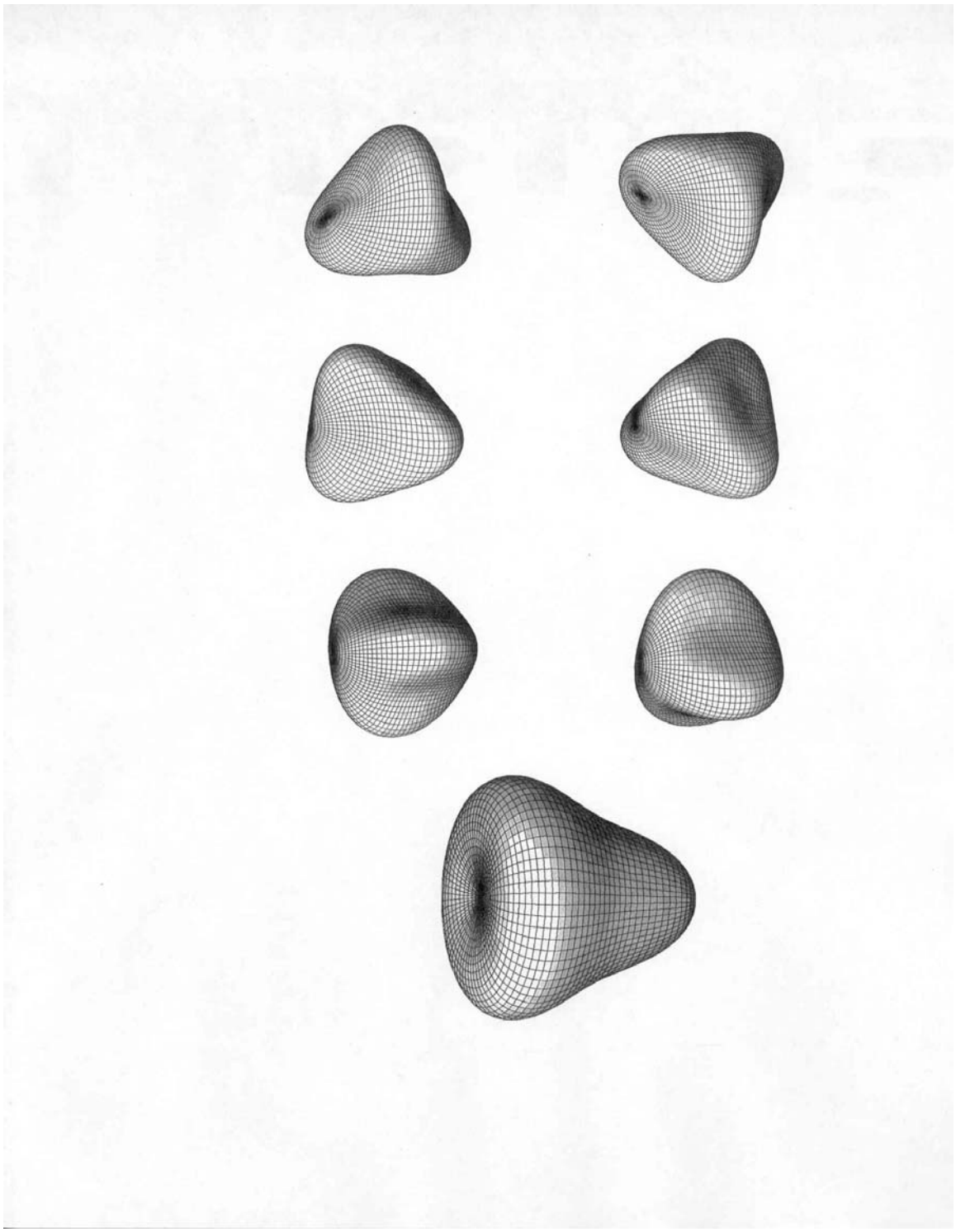

Figure 5.4 - Axisymmetric and Non-axisymmetric Mode Shapes for n=3, Lower Branch

Based upon comparisons of theoretical predictions and axisymmetric finite element simulations, ABAQUS predicts the axisymmetric natural frequencies of a spherical shell with high accuracy (The first 26 modes of the example investigated were all well within one percent of corresponding theoretical values).

Corresponding nonaxisymmetric modes of a complete spherical shell were also accurately predicted by ABAQUS. Results confirmed the existence of the 2n+1 linearly independent, degenerate modes at each discrete frequency value. These degenerate modes, according to Silbiger, have identical mode shape, but are independent because an axis of symmetry cannot be uniquely be specified for a complete, free spherical shell.

Calculations using ABAQUS for a similar containment vessel with nozzles revealed that frequencies were somewhat similar, as expected. However, each modal frequency was found to be distinct, as predicted by Silbiger, suggesting that mode shapes of nonaxisymmetric modes are unique in this case.

6.0 SUMMARY

High explosive containment vessels are typically subjected to both impulsive pressure loading as well as quasi-static pressure buildup. An example spherical containment vessel subjected to transient impulsive pressure loading is analyzed by methods appropriate to this loading. It is illustrated that because of inertia effects, the analysis of containment vessels to only the effects of static pressure loading is invalid. Inertia effects need to be included in the determination of peak structural response. Non-spherical containment vessels are widely used as well, and the same underlying principles are generally applicable to differing vessel geometries.

The effects of non-symmetric explosive detonations are also investigated. It is concluded, based upon the studies reported, that it is difficult to draw general conclusions regarding the influence of asymmetric loading, whether from an off-center-initiated charge or from a charge placed off center in the vessel. In most cases, response (peak stress/strain) does increase for asymmetric loading, however.

Vibrations of spherical Containment Vessels are described. The superposition and interaction of different modes of response with closely-spaced frequencies is shown to result in late-time 'strain growth' in these vessels.

ACKNOWLEDGMENTS

The authors are grateful to the following PVRC Reviewers for providing helpful comments and recommendations on this report: Keshab K. Dwivedy, Henry H. Hwang, Paul Bezler, John C. Minichiello, George Miller, Robert Forgan, and Dr. Robert Nickell. The authors also thank Jerry Bitner and Greg Hollinger for their support and assistance on all aspects of this report.

REFERENCES

1. A.M. Clayton, "Design Methods Used for AWE Containment Vessels", **Welding Research Council Progress Reports**, Vol. LVI, No. 11/12, Welding Research Council, New York, Nov/Dec 2001 (See also: A. M. Clayton and R. Forgan, "The Design of Steel Vessels to Contain Explosions," **2000 ASME Pressure Vessels and Piping Conference**, Seattle, WA, July 2000).

2. R. Moehrle, M. Chiesa, B. Haroldsen, and J. Dike, "Vessel Life Cycle Analysis of the Explosive Destruction System (EDS) - A System to Destroy Legacy Chemical Weapons," **2001 ASME Pressure Vessels and Piping Conference**, Atlanta, GA, July 2001.

3. R. R. Karpp, T. A. Duffey, and T. R. Neal, "Response of Containment Vessels to Explosive Blast Loading**," Journal of Pressure Vessel Technology**, Vol. 105, pp. 23-27 (1983).

4. J. J. White and B. D. Trott, "Scaling Law for the Elastic Response of Spherical Explosion-Containment Vessels," **Experimental Mechanics**, Vol. 20, No. 5, May 1980, pp. 174-177.

5. W. E. Baker, W. C. L. Hu, and T. R. Jackson, "Elastic Response of Thin Spherical Shells to Axisymmetric Blast Loading," **Journal of Applied Mechanics**, Vol. 33, December 1966, pp. 800–806.

6. A. A. Buzukov, "Characteristics of the Behavior of the Walls of Explosion Chambers under the Action of Pulsed Loading," **Fizika Goreniya i Vzryva**, Vol. 12, No. 4, July-Aug. 1976, pp. 605-610.

7. W. E. Baker, "The Elastic-Plastic Response of Thin Spherical Shells to Internal Blast Loading," **Journal of Applied Mechanics**, Vol 27, No. 1, Mar. 1960, pp. 139-144.

8. A. F. Demchuk, "Method for Designing Explosive Chambers," **Zhurnal Prikladnoi Mekhaniki i Technicheskoi Fiziki**, Vol 9, No. 5, 1968, pp. 47-50.

9. A. G. Ivanov, S. A. Novikov, and V. A. Sinitsyn, "The Behavior of Steel Shells When Charges of Explosive Detonate Inside Them," **Zhurnal Prikladnoi Mekhaniki i Technicheskoi Fiziki**, Vol. 9, No. 6, 1968, pp. 94-98.

10. B. D. Trott, J. E. Backofen, J. J. White, and J. Petty, "Design of Explosive Blast Containment Vessels for Explosive Ordnance Disposal Units," **Proceedings of the Army Symposium on Solid Mechanics, *1978***, Army Materials and Mechanics Research Center, AMMRC MS 78-3, Watertown, Mass, Sept. 1978, pp. 215-228.

11. J. M. Biggs, **Introduction to Structural Dynamics** (McGraw-Hill, New York, 1964).

12. R. T. Karpp, T. A. Duffey, and T. R. Neal, **Response of Containment Vessels to Explosive Blast Loading**, Los Alamos Scientific Laboratory report LA-8082, June 1980.

13. R. L. Martineau, **HSLA-100 Test Series Structural Analysis and Experimental Comparisons for Vessel Certification,** Los Alamos National Laboratory document, Report No. DX-5:99-013, May 27, 1999.

14. S. T. Bennion and S. P. Clancy, **MESA-2D**, Version 5, LA-CP-92-229, Los Alamos National Laboratory, June 1992.

15 **LS-DYNA Users Manual**, Version 950, Livermore Software Technology Corporation, Livermore, CA, May 1999.

16. R. R. Stevens and S. P. Rojas, **Confinement Vessel Dynamic Analysis**, Los Alamos National Laboratory Report LA-13628-MS, August 1999.

17. E. S. Hertel, et al., "CTH A Software Family for Multi-Dimensional Shock Physics Analysis," **Proc. 19th International Symposium on Shock Waves**, Vol. 1, p. 377, July 1993.

18. A. I. Belov, V. E. Klapovskii, V. A. Kornilo, V. N. Mineev, and V. S. Shiyan, "Dynamics of a Spherical Shell Under a Nonsymmetric Internal Pulse Loading," **Fizika Goreniya I Vzryva**, Vol. 20, No. 3, pp. 71–74, May-June 1984.

19. R. Stevens, **Confinement Vessel HE Eccentricity Study**, Los Alamos National Laboratory Memorandum ESA-EA:00-008, Jan 14, 2000.

20. J. A. Zukas and W. P. Walters, **Explosive Effects and Applications**, Springer Verlag, New York, NY, 1998.

21. P. W. Cooper, **Explosives Engineering**, VCH Publishers, New York, NY, 1996.

22. W. E. Baker, **Explosions in Air**, 2nd Edition, WE Baker Engineering, San Antonio, TX, 1983.

23. W. Fickett and W. C. Davis, **Detonations; Theory and Experiment**, Dover Publications Inc., NY, 1979.

24. Departments of the US Army, US Navy, and US Air Force, **Structures to Resist the Effects of Accidental Explosions**, Report AD-A243-272, US Army TM 5-1300, US Navy NAVFAC P-397, US Air Force AFR 88-22, November 1990.

25. United States Department of Energy, **A Manual for the Prediction of Blast and Fragment Loadings on Structures**, DOE/TIC-11268, US Department of Energy, Albuquerque Operations Office, Amarillo Area Office, Pantex Plant, November 1980.

26. Headquarters, US Department of the Army, Technical Manual TM 5-855-1, **Fundamentals of Protective Design for Conventional Weapons**, US Army, 1986.

27. M. L. Wilkins, **Computer Simulation of Dynamic Phenomena**, Springer-Verlag, New York, 1992.

28. **AUTODYN 2-D/3-D, I**nteractive Non-Linear Dynamics Analysis Software, Century Dynamics, Inc.

29. A. Whenhui, X. Honglu, A. Guangquan, and G.K. Schleyer, "Dynamic Response of Cylindrical Explosive Chambers to Internal Blast Loading Produced by a Concentrated Charge", **International Journal of Impact Engineering**, **19**, 1997, pp. 831-845.

30. W.E. Baker, "Axisymmetric Modes of Vibration of Thin Spherical Shell", **Journal of the Acoustical Society of America**, **33**, 1961, pp. 1749-1758.

31. H. Lamb, "On the Vibrations of a Spherical Shell", **Proceedings of the London Mathematical Society**, **XIV**, 1883, p. 50.

32. A. Silbiger, "Nonaxisymmetric Modes of Vibration of Thin Spherical Shells", **Journal of the Acoustical Society of America**, **38**, 1965, pp. 367-368.

33. A. Kalnins, "Effect of Bending on Vibrations of Spherical Shells", **Journal of the Acoustical Society of America**, **36**, 1964, pp. 74-81.

34. F.I. Niordson, "Free Vibrations of Thin Elastic Spherical Shells", **International Journal of Solids and Structures**, **20**, 1984, pp. 667-687.

35. J.P. Wilkinson, "Natural Frequencies of Closed Spherical Shells", **Journal of the Acoustical Society of America**, **38**, 1965, pp. 367-368.

36. A.H. Shah, C.V. Ramkrishnan, and S.K. Datta, "Three-Dimensional and Shell-Theory Analysis of Elastic Waves in a Hollow Sphere**", Journal of Applied Mechanics**, **36**, 1969, pp. 431-439.

37. T. Hirai and M. Kuroda, "Analysis of Natural Vibrations of a Spherical Shell with Variable Thickness", **Journal of the Acoustical Society of America**, **86**, 1989, pp. 1864-1875.

38. R.B. Evans, "Modal Impedances for Nonaxisymmetric Vibrations of a Thin Spherical Shell", **Journal of the Acoustical Society of America**, **100**, 1996, pp. 1242-1245.

39. Anon., **ABAQUS/Standard Example Problems Manual**, Hibbitt, Karlsson and Sorenson, Inc., 1997, pp. 3.1.1-1 - 8.

40. F.I. Niordson, "The Spectrum of Free Vibrations of a Thin Elastic Spherical Shell", **International Journal of Solids and Structures**, **24**, 1988, pp. 947-961.

41. R.D. Blevins, **Formulas for Natural Frequency and Mode Shape**, Krieger Publishing Co., 1984, pp. 328-330.

42. T.A. Duffey, W.E. Baker, B.B. Lewis and J.M. Greene, "Containment of Explosions in Spherical Shells", Presented at ASME Pressure Vessel and Piping Conference, July 1993, **Piping Supports and Structural Dynamics** (A. Dermenjian, Ed.), ASME PVP**, 264,** 1993.

43. Martineau, R., Los Alamos National Laboratory, Personal Communication, May 27, 1999.